# Development and application of a simulator for Offshore Wind Turbine Blades Installation

Zhengru Ren[a,b,c], Zhiyu Jiang[a,c,*], Roger Skjetne[a,b,c], Zhen Gao[a,b,c]

*[a]Centre for Research-based Innovation of Marine Operations (SFI MOVE)*
*[b]Centre for Autonomous Marine Operations and Systems (AMOS)*
*[c]Department of Marine Technology, Norwegian University of Science and Technology (NTNU), NO-7491 Trondheim, Norway*

---

**Abstract**

In an offshore environment, offshore wind energy resources are more available and stable, but the investment cost is much higher than that of onshore wind. The installation cost is a crucial factor of the investment. With the increasing number of planned and approved offshore wind farms, offshore wind turbine installation and relevant operations have received tremendous attention. Therefore, expediting the turbine-structure mating operations through a higher level of automation in offshore wind turbine installations may provide important economic benefits. To achieve a higher automation level and reduce the weather waiting time during the installation of offshore wind turbines, a flexible simulation-verification framework with high fidelity is needed. However, state-of-the-art wind turbine numerical analysis code is neither convenient nor open enough for applications concerning the design and verification of control algorithms. MATLAB/Simulink is among the most widely utilized numerical platforms by control engineers and researchers. This paper describes the development of a modularized blade installation simulation toolbox for the purpose of control design in MATLAB/Simulink. The toolbox can be used to simulate several blade installation configurations, both onshore and offshore. The paper presents the key features and equations of the different modules, exemplified by a single blade installation operation. Code-to-code verification results are presented and discussed with both quasi-steady wind and three-dimensional turbulent wind field.

*Keywords:* Offshore installation; Blade installation; Simulation model; MATLAB® and Simulink®.

---

## 1. Introduction

With the growing interest and need for clean energy, wind energy has become increasingly popular in recent years. Wind turbines are categorized into onshore wind turbines and offshore wind turbines (OWTs) based on their installation locations. Because of their high initial installation and lifespan maintenance costs, the price of offshore wind energy remains more than three times higher than onshore wind energy[1]. Installation expenses significantly influence the cost of offshore wind energy. Hence, techniques that can make the OWT installation more efficient are of great value.

For wind turbine blade installation, several approaches have been developed. For example, assembled rotor installation, bunny-ear configuration, and single blade installation are often used [2?, 3]. The selection among these approaches is a trade-off among the equipment capacity, number of offshore lifting operations, weather, etc. All these factors influence the offshore operational time, deck usage, and the overall installation cost. As the example of this paper, single blade installation is a wind turbine blade installation method that is especially suitable for large-scale OWTs, as individual lifts of the blades are much easier than maneuvering of a full rotor-tower-nacelle assembly offshore. This method also facilitates deck usage and requires low crane capacity of the installation vessel. Blades are lifted and mated separately. When the weather conditions allow the operation, one blade is held by a yoke and lifted by a crane from the deck, with the blade root approaching the hub. After moving the blade to the mating position at the hub, the mating operation proceeds if the blade root motion is limited within a specified range. The single blade installation approach provides a more efficient deck utilization and reduces the transportation time, for instance, by allowing more turbine components to be carried in one trip. The disadvantage is that this installation approach typically requires more operation time. Using state-of-the-art lift equipment, the single blade installation approach is only allowed to be conducted up to a mean wind speed of approximately $8-12$ m/s at the hub height [4]. Hence, increasing the weather window for the installation work and making the lifting operation more time efficient will greatly reduce the installation costs.

---

*Corresponding author
Email addresses:* `zhengru.ren@ntnu.no` (Zhengru Ren), `zhiyu.jiang@ntnu.no` (Zhiyu Jiang), `roger.skjetne@ntnu.no` (Roger Skjetne), `zhen.gao@ntnu.no` (Zhen Gao)

Research on intelligent marine operations are seeing increasing attention [5–10]. The typical objectives are to enhance the overall efficiency, ensure safety, broaden the operating window, and, ultimately, gain economic benefits. Because single blade installation approach demands large amount of offshore working time, the installation cost can be reduced if the mating operations are accelerated by enhancing the automation level for the blade installation system. To the best of the authors' knowledge, no studies have looked into such issues. Therefore, there is an urgent need for highly efficient and user-friendly simulation tools for use during the controller design process for marine installations.

To start a control design for such a complex process as an OWT installation, a numerical model is surely needed. Open-source MATLAB/Simulink toolboxes, such as the MSS GNC and MSS Hydro toolboxes [11, 12] and MSS MarPowSim [13], are widely applied for marine control systems, e.g., the dynamic positioning of surface vessels and power management systems. However, these toolboxes lack modules to model wind turbine installations. Commercial software for marine operations, such as SIMA [14, 15], are widely used during analysis and design. However, their closed-source policy and tedious customization of external dynamic-link libraries (DLLs) for the design of control systems weaken their applicability to control design and analysis. State-of-the-art aeroelastic codes for designing of wind turbines under normal operations, including HAWC2 [16], FAST [17], and Bladed [18], are based on blade element momentum (BEM) theory. Complex aerodynamic performances, such as blade tip flow, wake dynamic inflow, and dynamic stall, are modeled. Code-to-code comprehensive simulations [19], prove that these codes agree well with each other. Single blade installation has been studied using HAWC2 [4, 20]. Taking HAWC2 as an example, although they can interface with MATLAB/Simulink through TCP/IP or use some DLLs to implement simple control laws, there are disadvantages. First, setting up the interface and debugging the model are often time consuming. Furthermore, limitations of the supported modules restrict its flexibility and complexity, except for the blade, during modeling. Other limitations include fixed time steps and cumbersome user interfaces. In addition, numerous codes and toolboxes, for example, wind turbine gearbox [21], a wind turbine sub-model in an in-house computational fluid dynamics (CFD) code [22], and a computational aeroelastic tool with the Boundary Element Method [23], have been developed that are relevant to wind turbine simulations. None of these, however, is able to simulate blade installation.

This paper presents the development of an open-source object-oriented simulation-verification blade installation modeling toolbox targeting the design and analysis of automation and control functions. The code is developed primarily for wind turbine blade installation, but it can also be used in related fields with simple modifications. The resulting functions and modules are integrated in the **MarIn** (**Mar**ine **In**stallation) toolbox, which is under development within the SFI MOVE center at NTNU. The modularized code in MATLAB/Simulink can be used in place of commercial software with verified numerical correctness.

The main contributions of this paper are the development of an object-oriented MATLAB/Simulink-based simulation verification toolbox for the blade installation of OWTs and a verification of the model against the mainstream commercial software HAWC2.

The paper is structured as follows. In Section 2, the problem formulation and development guidelines are proposed. In Section 3, relevant coordinate systems and coordinate transformations are introduced. The models of the wire ropes, winches, and hook are presented in Section 4. The blade dynamics, wind velocity with turbulence model, and wind-induced loads are presented in Section 5. Code-to-code verification with steady wind is conducted in Section 6 to confirm that the code calculates the correct aerodynamic loads acting on the blade. In Section 7, a single blade installation process is modeled as an example, and time-domain simulations are conducted to verify the model. Finally, the conclusion summarizes the paper.

**Notations**: In this paper, scalars, vectors, and matrices are denoted with normal lowercase letters, bold lowercase letters, and bold capital letters, respectively. $|\boldsymbol{x}|$ stands for the Euclidean norm, i.e., $|\boldsymbol{x}|^2 = \boldsymbol{x}^\top \boldsymbol{x}$. The overline $\bar{a}$ denotes the upper bound of a variable $a$, and $\boldsymbol{I}_n$ and $\boldsymbol{0}_n$ are the identity matrix and the zero matrix of size $n \times n$, respectively. A nomenclature is given Appendix A.

**Color codes in figures**: To avoid confusion, the colors in the following diagrams have the following meanings:

- Blue:     Coordinate frame

- Red:     Load (force/moment)

- Green:     Wind velocity

**Superscripts and subscripts**: Normally, the superscripts denote the coordinate systems. To simplify the expression, the global reference frame is adopted without any superscripts. The subscripts below have the following corresponding meanings:

- b     Blade

- h     Hook

- l    Lift wire

- m    Winch motor

- p    Pulley (crane tip)

- r    Wire rope

- s    Slings

- t    Tugger line

- TI  Turbulence intensity

- w    Wind

- y    Yoke

## 2. Blade installation framework

### 2.1. Description of single blade installation

In this section, a commonly used single blade installation configuration is introduced to help the reader understand the necessary components in the toolbox and the basic ideas utilized during the modeling of such a process. The configuration of a single blade lifting operation is depicted in Fig. 1. In this example, a monopile foundation is considered, which has been hammered into the seabed. The supporting structures, including the transition piece, tower, and hub, were assembled subsequently. A jackup installation vessel is assumed to be conducting the single blade installation operation. The vessel-mounted crane is responsible for lifting a blade by wire ropes. A lift wire connects the crane tip and the hook, and the hook connects to a yoke with slings. A turbine blade is held by the yoke and suspended in the air. Tugger lines connecting the crane boom to the yoke are used to reduce the blade's pendulum motion. The crane-wire-hook-blade system is exposed to a windy environment with both a mean wind load and dynamic wind loads.

When the weather window allows the installation to be conducted, the hub is first rotated to the desired orientation such that the flange holes on the hub are ready to mate with the guiding pins on the blade root, normally horizontally. Then, the blade is lifted from the deck to the hub elevation by controlling the boom winch and corresponding lift wire length. Afterward, the crane is rotated to move the blade horizontally to a position near the final mating point while the blade's motion is monitored. If the motion stays within the allowable range, the final mating operation is executed by manually inserting the guiding pins into the flange holes. After bolting the blade and the hub, the installation is finished.
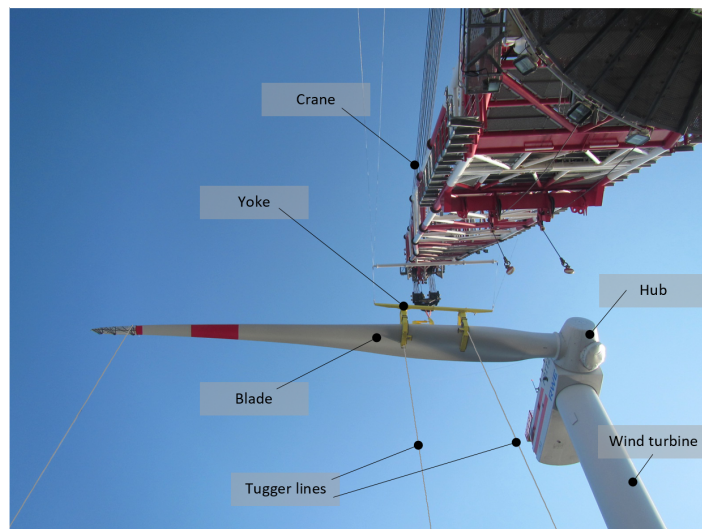


Figure 1: The mating phase during a single blade installation (Image source: RWE GmbH [24]).

During the mating process, if the relative motions between the blade root and hub are too large, guide pins can be damaged which causes unnecessary delays. Visual guidance is needed, and banksmen are often used to give orders to the crane operator and to assist the final mating process. The need for banksmen poses potential risks in such activities. If sensorial or automated guidance can be used to automate the process, such risks can be lowered substantially.

## 2.2. Model assumptions

From the above description, the main components of the blade installation process are

- Physical components: vessel, crane, winch, lift wires, slings, tugger lines, hook, yoke, blade;

- Environmental components: wind turbulence simulator, and wind-induced loads.

The proposed toolbox can be applied to simulation of blade installation using either a jackup or a floating vessel. To install blades with a jackup is a simplified scenario, and the crane boom is fixed in space. The simplified configuration is illustrated in Fig. 2. For a floating installation vessel, the real-time crane tip position can be calculated by a coordinate transformation of the vessel's position and orientations and the crane configuration. Because the wind-induced loads acting on a blade are substantially smaller than the vessel's inertial and gravity loads, the influence of the crane on the vessel is neglected. Given the light weight of the blade system (less than 100 tonnes), it is acceptable to assume that the load and load effects on the crane caused by its payload can be disregarded. The crane flexibility can be modeled which affects the stiffness of the rigging system and hence the wire tension. Normally, an equivalent stiffness of the wire rope can be used to model the crane flexibility, in which the crane flexibility can be considered together with the actual flexibility of the rope.

**Remark 1**: Note that for high-fidelity numerical models for engineering design and risk assessment, such effects should not be neglected and instead should be considered. However, for the purpose of control design, one can typically reduce the fidelity of the model by disregarding fast stable dynamics to produce a simplified model capturing the most important dynamics. The control system, with its actuators, will typically dominate the loads on the plant and make it behave according to the specified control objective. That is also why it is very important to include a realistic model of the control functions when performing detailed analysis of loads and load effects.

The length of the lift wire is a sum of the wire between the crane winch drum and the crane tip and the wire between the crane tip and the hook. Two slings connect the hook to the yoke. We assume that the crane, hook, and blade are all rigid bodies and that the yoke mass is located at the blade COG. The primary objectives for active turbine installation operations are to stabilize the payloads and to move the payloads with desired trajectories. Global loads and motion analysis are of importance, while the local structural analysis with attention on structural flexibility is disregarded. Therefore, the rigid-body dynamics are the focus instead of the BEM technique adopted by operational wind turbines.

The hook dynamics is modeled in 3 degrees of freedom (DOFs), and the blade motion is simulated in 6 DOFs. The NREL 5 MW reference turbine blade is taken as an example hereafter in this paper [25]. The mass of the yoke is concentrated at the COG of the blade. Two tugger lines are placed symmetrically about the blade COG on the yoke. The other ends of the tugger lines are fixed to the vessel, which moves with the vessel. Lift wires, slings, and tugger lines are modeled as tensile springs with specific damping coefficients, therein merely providing tension with a positive elongation.
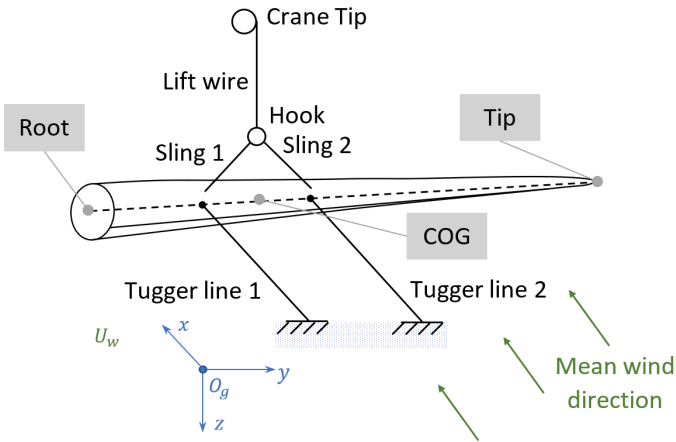


Figure 2: Single blade installation setup.

## 2.3. Toolbox overview

With the simplified assumptions, the main modules in this toolbox correspond to the vessel, crane, wire rope, hook, blade, wind generator, and wind-induced loads. The proposed toolbox consists of a framework to simulate the blade installation with a relatively high fidelity for control design purposes. The modeling procedure is object oriented, therein

interconnecting blocks with Newton-Euler mechanics. All components should be easy to assemble to achieve different configurations. The inputs/outputs (I/O) are tabulated in Tables A.5-A.10; see Appendix C for more details.

The configuration of an example system is presented in Fig. 3. The vessel is an optional component for offshore wind turbine blade installation. For an installation operation conducted with a floating vessel, the position of the crane tip and the ends of the tugger lines are movable. For simulating an installation using a jackup vessel rigidly fixed to the seabed, the vessel model is skipped, and the boundary conditions of the crane tip and the tugger lines are imposed. The crane tip and the hook are the ends of a lift wire. The restoring force can be calculated based on the elongation and stiffness. The same calculations are applied to the slings and the tugger lines. The total force acting on the hook is the restoring force from the lift wire and slings by disregarding the wind-induced loads. The external loads acting on the blade are the wind-induced loads and restoring forces from the corresponding connected wires.

The proposed toolbox is able to model not only single blade installation but also other complex installation configurations. With the combination of individual blade modules, bunny-ear configuration and assembled rotor configurations are realizable by fixing the root end to a hub or rotor, which is modeled as a point mass. The external wind-induced loads acting on the entire payload can then be calculated.
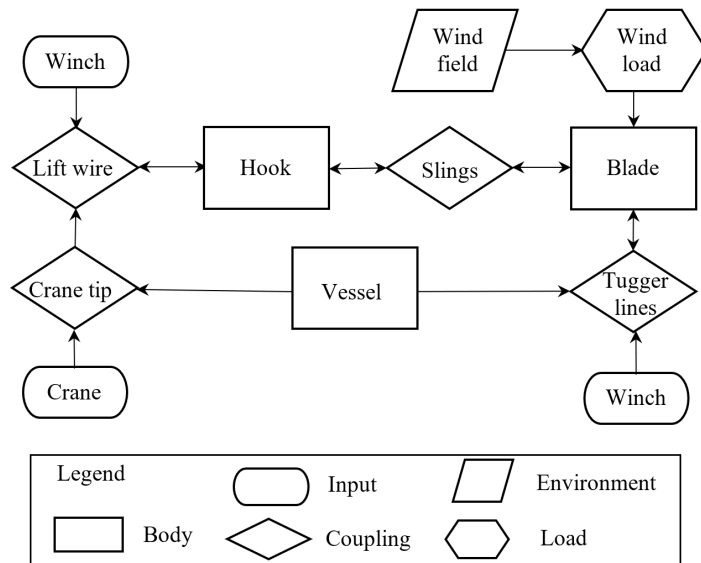


Figure 3: Model overview.

## 3. Coordinate systems and coordinate transformation

### 3.1. Coordinate systems

We use the convention that all the coordinate systems follow the right-hand rule. To sum up the wind-induced load, the blade is divided into $n$ segments with $n + 1$ nodes along the span. The blade root and tip are nodes numbered with 0 and $n$, respectively. The wind turbulence data are pre-calculated information in a box-shape structure, where the wind box runs in its length direction.

Four coordinate systems are briefly defined as follows:

- Global north-east-down (NED) geographic coordinate system $\{N\}$: The origin $O_n$ is placed on the free sea surface with the $x$-axis pointing to the north, $y$-axis pointing to the east, and $z$-direction being downward. The orientations about the $x$-, $y$-, and $z$-axes are roll ($\phi$), pitch ($\theta$), and yaw ($\psi$), respectively. NED is assumed to be an inertia frame.

- Blade body-fixed frame $\{B\}$: The origin $O_b$ is placed at the blade COG. The $y^b$-axis points from the root center to the tip center in the spanwise direction, and the $x^b$-axis is directed from the leading edge to the trailing edge in the chordwise direction. The angular velocities about the $x^b$-, $y^b$-, and $z^b$-axes are $p$, $q$, and $r$, respectively. Note that the $y$-axis is chosen as the longitudinal axis along the blade so that rotation about $y$ results in a blade pitch angle, being consistent with the blade pitch during turbine operation.
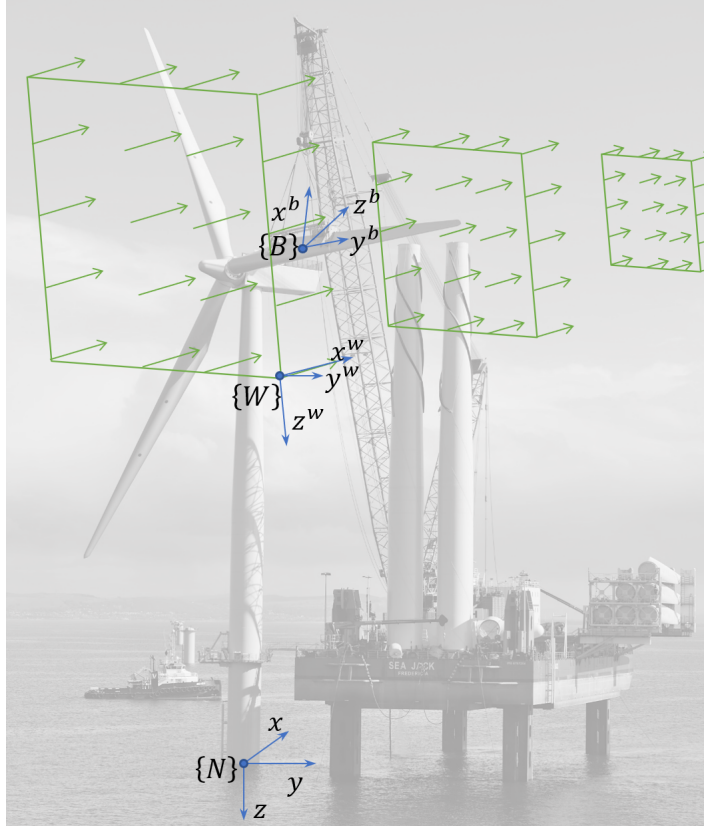
Figure 4: Global, body-fixed, and mean-wind coordinate systems for the blade installation model (Image source: HeavyLiftNews).

- Aerodynamic frame at node $i \in \{0, 1, \cdots, n\}$ in the body-fixed frame $\{B_i\}$: The origin $O_{bi}$ is at the geometric center of the blade $i^{th}$ cross section. The $y^{bi}$-axis shares the same direction as the $y^b$-axis. The $x^b$-axis and $z^b$-axis are considered as a combination of a planar translation and a rotation about the $y^b$-axis. The aerodynamic twist, i.e., the angle between $x^{bi}$ and $x^b$, is denoted by $\theta_{y,i}$.

- Mean-wind coordinate system $\{W\}$: The origin $O_w$ is located at the lower-right corner of the wind turbulence box. $O_w$ is placed at a preset point in $\{N\}$. The $x^w$-axis points in the wind inflow direction, i.e., the box's length, and $z^w$ is directed downward, i.e., the box's height. The wind velocities in the $x^w$-, $y^w$-, and $z^w$-axes are $u_w$, $v_w$, and $w_w$, respectively. The box orientation about $\{N\}$ is constant, i.e., $\phi_w$, $\theta_w$, and $\psi_w$ are constants.

The NED reference frame is a widely used coordinate system in ocean engineering, such as, the control of dynamic positioning vessels, moored vessels, autonomous underwater vehicles (AUVs), and remotely operated vehicles (ROVs). The blade body-fixed frame is also called the main-body coordinate system. The configuration is shown in Figs. 4-5. The wind shear is not considered. For the single blade horizontally positioned, the vertical variation in wind speed due to wind profile is not important, since the blade vertical movement is limited.

**Remark 2**: The reference frames $\{B_i\}$ are only used to compute the aerodynamic loads; these frames otherwise do not enter the calculation loop.

**Remark 3**: Euler angles are used to show the rotation relation between the coordinate frames. Rotations about the fixed $x$-, $y$-, and $z$-axes are named roll, pitch, and yaw. For the sake of consistency and clarity, the roll, pitch, and yaw are denoted by $\phi$, $\theta$, and $\psi$, respectively, regardless of the coordinate systems. The variables in the above-mentioned reference frames are tabulated in Table 1.

### 3.2. Transformation between coordinate systems

A vector, position or translational velocity is transformed between the coordinate systems, from $\{B\}$ to $\{A\}$, by multiplying by the rotation matrix $\boldsymbol{R}_b^a$, i.e.,

$$\boldsymbol{v}^a = \boldsymbol{R}_b^a(\boldsymbol{\Theta}_{ab})\boldsymbol{v}^b, \tag{1}$$
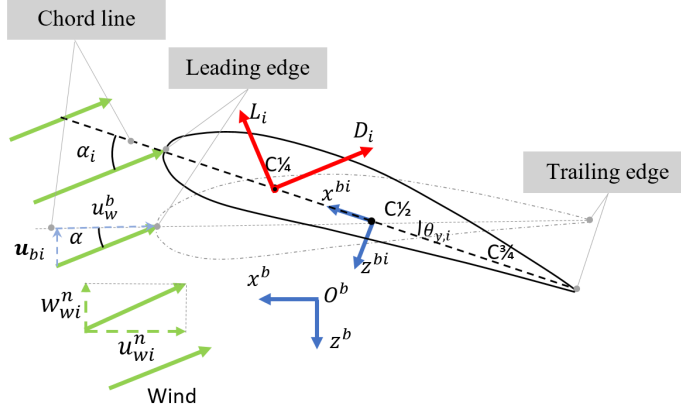
Figure 5: Body-fixed and aerodynamic coordinate systems. The solid line and the dashed line are the outline of the $i^{th}$ blade element with and without rotation $\theta_{y,i}$, respectively.

where $\boldsymbol{v}^a$ and $\boldsymbol{v}^b \in \mathbb{R}^3$ are two vectors in $\{A\}$ and $\{B\}$, $\boldsymbol{\Theta}_{ab}$ denotes a vector of the Euler angles between $\{A\}$ and $\{B\}$, and the rotation matrix $\boldsymbol{R}_b^a$ rotates from the coordinate system $\{B\}$, expressed by the subscript, to the frame $\{A\}$, denoted by the superscript. The inverse transformation is given by the matrix $\boldsymbol{R}_b^a(\boldsymbol{\Theta}_{ab})^{-1} = \boldsymbol{R}_b^a(\boldsymbol{\Theta}_{ab})^\top = \boldsymbol{R}_a^b(\boldsymbol{\Theta}_{ab})$.

In this paper, the following order is adopted to transform a vector from one frame to another: $\{W\} \leftrightarrow \{N\} \leftrightarrow \{B\} \leftrightarrow \{B_i\}$. The transformations are bidirectional. Therefore, the wind velocity is transformed to the aerodynamic frame to represent the realistic wind-induced loads by three transformations, i.e., first from $\{W\}$ to $\{N\}$, then from $\{N\}$ to $\{B\}$, and finally from $\{B\}$ to $\{B_i\}$. The relations between the vectors in the above-mentioned coordinate systems are tabulated in Table 2. The variables $\boldsymbol{R}_b^n$ and $\boldsymbol{R}_w^n$ are short for $\boldsymbol{R}_b^n(\boldsymbol{\Theta}_{bn})$ and $\boldsymbol{R}_w^n(\boldsymbol{\Theta}_{wn})$, respectively.

Additionally, position transformations between the coordinate systems are expressed by

$$\{B\} \rightarrow \{N\}: \qquad \boldsymbol{p} = \boldsymbol{R}_b^n \boldsymbol{p}^b + \boldsymbol{d}_b^n, \tag{2}$$
$$\{W\} \rightarrow \{N\}: \qquad \boldsymbol{p} = \boldsymbol{R}_w^n \boldsymbol{p}^w + \boldsymbol{d}_w^n, \tag{3}$$

where the distance vectors between the coordinate origins are

$$\boldsymbol{d}_b^n = -\boldsymbol{d}_n^b = \boldsymbol{p}_{O_n} - \boldsymbol{p}_{O_b}, \tag{4}$$
$$\boldsymbol{d}_w^n = -\boldsymbol{d}_n^w = \boldsymbol{p}_{O_n} - \boldsymbol{p}_{O_w}, \tag{5}$$

with $\boldsymbol{p}_{O_n} = [x_{O_n}, y_{O_n}, z_{O_n}]^\top$, $\boldsymbol{p}_{O_b} = [x_{O_b}, y_{O_b}, z_{O_b}]^\top$, and $\boldsymbol{p}_{O_w} = [x_{O_w}, y_{O_w}, z_{O_w}]^\top$.

$$\tag{6}$$

## 4. Ropes, winches, and hook

### 4.1. Wire rope, sling, and tugger line

The lift wires, slings, and tugger lines are modeled as tensile springs, which only provide tension when the axial elongation is positive. The self weight of the rope is disregarded. Without loss of generality, a tensile spring between points $A$ and $B$, with an initial length $\bar{l}_{AB}$ between points $A$ and $B$, is presented as an example. Define $\boldsymbol{l}_{AB} = \boldsymbol{p}_A - \boldsymbol{p}_B$,

Table 1: Variables in the corresponding frame

|  | Position in | Relative orientation to $\{n\}$ | Translational velocity | Angular velocity |
|---|---|---|---|---|
| $\{N\}$ | $\boldsymbol{p} = [x, y, z]^\top$ | - | $\boldsymbol{v}_n = [\dot{x}, \dot{y}, \dot{z}]^\top$ | - |
| $\{B\}$ | $\boldsymbol{p}^b = [x^b, y^b, z^b]^\top$ | $\boldsymbol{\Theta}_{bn} = [\phi, \theta, \psi]^\top$ | $\boldsymbol{v}_b = [u, v, w]^\top$ | $\boldsymbol{\omega}_b = [p, q, r]^\top$ |
| $\{W\}$ | $\boldsymbol{p}^w = [x^w, y^w, z^w]^\top$ | $\boldsymbol{\Theta}_{wn} = [\phi_w, \theta_w, \psi_w]^\top$ | $\boldsymbol{v}_w = [u_w, v_w, w_w]^\top$ | - |

7

Table 2: Vector transformation among the above-mentioned coordinate systems. In the table, $\boldsymbol{a} = (\cdot)\boldsymbol{b}$.

| $\boldsymbol{a}$ \ $\boldsymbol{b}$ | $\boldsymbol{\nu}^n$ | $\boldsymbol{\nu}^b$ | $\boldsymbol{\nu}^w$ |
|---|---|---|---|
| $\boldsymbol{\nu}^n =$ | $\boldsymbol{I}_3$ | $\boldsymbol{R}_b^n$ | $\boldsymbol{R}_w^n$ |
| $\boldsymbol{\nu}^b =$ | $\boldsymbol{R}_b^{n\top}$ | $\boldsymbol{I}_3$ | $\boldsymbol{R}_b^{n\top}\boldsymbol{R}_w^n$ |
| $\boldsymbol{\nu}^w =$ | $\boldsymbol{R}_w^{n\top}$ | $\boldsymbol{R}_w^{n\top}\boldsymbol{R}_b^n$ | $\boldsymbol{I}_3$ |

where $\boldsymbol{p}_A$ and $\boldsymbol{p}_B \in \mathbb{R}^3$ are the positions of the ends of the wire. If the mass of the wire rope is negligible, the restoring force [26] in the global frame, $\boldsymbol{f}_A \in \mathbb{R}^3$, is modeled as

$$\boldsymbol{f}_A = -\left(\kappa(\delta_{AB})k_r\delta_{AB} - d_r\frac{d\,\delta_{AB}}{d\,t}\right)\frac{\boldsymbol{l}_{AB}}{|\boldsymbol{l}_{AB}|}, \tag{7}$$

where $\frac{\boldsymbol{l}_{AB}}{|\boldsymbol{l}_{AB}|}$ decomposes the total force into three components in the NED frame. The restoring acting coefficient $\kappa$ is

$$\kappa(\delta_{AB}) = \begin{cases} 1 & \delta_{AB} \geq 0, \\ 0 & \text{otherwise.} \end{cases} \tag{8}$$

The axial elongation is

$$\delta_{AB} = |\boldsymbol{l}_{AB}| - \bar{l}_{AB}. \tag{9}$$

The elastic stiffness of the wire rope $k_r$ is a function of its length, as well as the characteristics of the wire rope, e.g., material, diameter, and strand construction, given by [26]

$$k_r = \gamma_r\frac{EA_r}{l_1}, \tag{10}$$

where $E$ denotes the Young's modulus, $A_r$ refers to the cross-sectional area of the rope, and $l_1$ is the overall initial length of the rope. For a lift wire or a tugger line, the initial overall length is $l_1 = l_l(\text{or } l_t) = \bar{l}_{AB} + l_0$, where $l_0$ is the length of the rope between the corresponding winch and pulley, which is assumed to be a constant. For a sling, there is no connected winch, i.e., $l_1 = l_s = \bar{l}_{AB}$. To sum up,

$$l_1 = \begin{cases} \bar{l}_{AB} + l_0 & \text{lift wire/tugger line,} \\ \bar{l}_{AB} & \text{sling.} \end{cases} \tag{11}$$

A general form of the modified coefficient for a stranded wire $\gamma_r$ is deduced in [27], given by

$$\gamma_r = \sum_{i=0}^{n_r}\frac{z_{ri}\cos^3\alpha_{ri}}{1 + v_{ri}\sin^2\alpha_{ri}}E_{ri}A_{ri}, \tag{12}$$

where $n_r$ is the number of wire layers counted from the inside, with $i = 0$ for the center wire, and $z_{ri}$, $E_{ri}$, $A_{ri}$, $\alpha_{ri}$, and $v_{ri}$ are the number of wires in layer $i$, the Young's modulus, the cross-sectional area, the lay angle, and the Poisson ratio of a wire in the the $i^{th}$ wire layer, respectively. A specific example of Eqn. (12) is $\gamma_r = \frac{\cos^3\alpha_r}{1+v_r\sin^2\alpha_r}$ when all the strands share the same lay angle and Poisson ratio.

The tension on the rope is $f_r = |\boldsymbol{f}_A|$. According to Newton's third law, the reaction force at the other end of the rope is

$$\boldsymbol{f}_B = -\boldsymbol{f}_A. \tag{13}$$

This rope model is implemented in the MarIn module called `Lifting equipment/Wire rope`.

*4.2. Winch*

A winch is connected at the end of a lift wire or a tugger line. The winch rotational acceleration is based on the friction, external load acting on the wire, and the torque input acting on the winch [28]. The external load is positive or zero. The winch model is given by

$$\dot{l}_1 = r_m\omega_m, \tag{14a}$$

$$\dot{\omega}_m = \frac{1}{J_m}\left(-d_m\omega_m + f_r r_m + T_m\right), \tag{14b}$$

where $\omega_m$ denotes the angular velocity of the winch motor, $r_m$ is the radius of the winch motor, $J_m$ represents the moment of inertia of the winch, $d_m$ refers to the damping coefficient of the torsional damper, and $T_m$ is the torque acting on the winch by the motor (usually viewed as the control input to the winch).

This winch dynamics is implemented in the MarIn module called `Lifting equipment/Winch`.

*4.3. Hook*

The hook is modeled as a 3-DOF rigid-body point. All the forces act on the COG. The gravity is not negligible; therefore, the mass of the hook, $m_h$, should be considered. Air resistance is negligible. The kinetic model of the hook, presented in Fig. 6, is given by Newton's second law according to

$$\dot{\boldsymbol{p}}_h = \boldsymbol{v}_h, \tag{15a}$$

$$\boldsymbol{M}_h \dot{\boldsymbol{v}}_h = \boldsymbol{g}_h + \sum_{i=1}^{n_l} \boldsymbol{f}_{li_B} + \sum_{i=1}^{n_s} \boldsymbol{f}_{si_A}, \tag{15b}$$

where $\boldsymbol{p}_h$ and $\boldsymbol{v}_h \in \mathbb{R}^3$ are the position and velocity vectors of the hook mass center in the global reference $\{N\}$, $\boldsymbol{M}_h = \text{diag}\{m_h, m_h, m_h\}$ is the hook mass matrix, $\boldsymbol{g}_h = [0, 0, m_h g]^\top$ is the hook gravity vector, $n_l$ and $n_s$ are the numbers of the connected lift wires and slings, and $\boldsymbol{f}_{li_B}$ and $\boldsymbol{f}_{si_A}$ are the restoring forces acting on the hook from the lift wires and slings in $\{N\}$, respectively. The subscripts $A$ and $B$ are used to distinguish the pair of reacting forces at both ends of a rope. To remain consistent, the higher points are labeled A, and the lower points are labeled B. See Fig. 6 for an illustration.

This hook dynamics is implemented in the MarIn module called `Lifting equipment/Hook`.
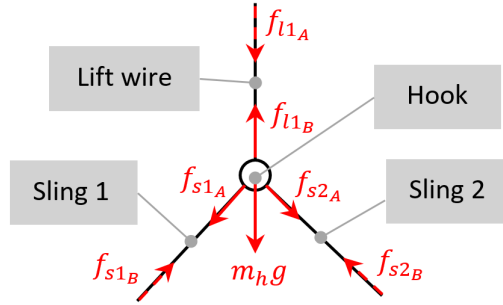


Figure 6: Free-body diagram of the lift wire and hook.

# 5. Blade dynamics

It is assumed that the mass of the yoke concentrates on the COG of the blade, and the moment of inertia of yoke is disregarded. Hence, the blade and the yoke are considered as one body. Hereafter, the blade dynamics is the dynamic of the entire blade-yoke system.

*5.1. Blade 6DOF kinematics*

The kinematic dynamics for the blade [29] is given by

$$\dot{\boldsymbol{\eta}}_b = \boldsymbol{J}(\boldsymbol{\Theta}_{bn})\boldsymbol{\nu}_b \tag{16}$$

$$\boldsymbol{J}(\boldsymbol{\Theta}_{bn}) = \begin{bmatrix} \boldsymbol{R}_b^n(\boldsymbol{\Theta}_{bn}) & \boldsymbol{0}_{3\times 3} \\ \boldsymbol{0}_{3\times 3} & \boldsymbol{T}(\boldsymbol{\Theta}_{bn}) \end{bmatrix} \tag{17}$$

where $\boldsymbol{J} \in \mathbb{R}^{6\times 6}$ is a transformation matrix and

$$\boldsymbol{\eta}_b = \begin{bmatrix} \boldsymbol{p}_n \\ \boldsymbol{\Theta}_{bn} \end{bmatrix}, \ \boldsymbol{\nu}_b = \begin{bmatrix} \boldsymbol{v}_b \\ \boldsymbol{\omega}_b \end{bmatrix}. \tag{18}$$

This rotation matrix is implemented in the MarIn module called `Basic functions/Euler angles to rotation matrix (z-y-x)`.

### 5.1.1. Blade rotation matrix

Three Euler angles are sufficient to represent an arbitrary rotation in 3D space. There are 12 sequences to do this. However, the rotation matrix is singular when the second orientation equals $\pm 90°$, namely, the gamble lock. Instead of the widely applied roll-pitch-yaw sequence [30], the rotation sequence is modified in case of a singularity of the rotation matrix. For a blade installation process, the yaw angle and pitch angle may practically become $\pm 90°$. In addition, it is reasonable to assume that the blade span would not be assembled vertically, i.e., the roll angle would not reach $\pm 90°$. Therefore, the rotation matrix for the blade is based on a pitch-roll-yaw sequence, and the rotation matrix from the body-fixed frame $\{B\}$ to the global frame $\{N\}$ becomes

$$
\begin{aligned}
\boldsymbol{R}_b^n(\boldsymbol{\Theta}_{bn}) &= \boldsymbol{R}_{z,\psi}\boldsymbol{R}_{x,\phi}\boldsymbol{R}_{y,\theta} \\
&= \begin{bmatrix} c\psi & -s\psi & 0 \\ s\psi & c\psi & 0 \\ 0 & 0 & 1 \end{bmatrix} \begin{bmatrix} 1 & 0 & 0 \\ 0 & c\phi & -s\phi \\ 0 & s\phi & c\phi \end{bmatrix} \begin{bmatrix} c\theta & 0 & s\theta \\ 0 & 1 & 0 \\ -s\theta & 0 & c\theta \end{bmatrix} \\
&= \begin{bmatrix} c\psi c\theta - s\psi s\phi s\theta & -s\psi c\phi & c\psi s\theta + s\psi s\phi c\theta \\ s\psi c\theta + c\psi s\phi s\theta & c\psi c\phi & s\psi s\theta - c\psi s\phi c\theta \\ -c\phi s\theta & s\phi & c\phi c\theta \end{bmatrix}.
\end{aligned}
\tag{19}
$$

Moreover, the wind-induced load transformation from $\{B\}$ to $\{B_i\}$ is defined by

$$
\boldsymbol{R}_b^{wi} = \boldsymbol{R}([0,\alpha,0]^\top),
\tag{20}
$$

where $\alpha$ is the angle of attack (AOA) of the dashed airfoil outline without aerodynamic twist $\theta_{y,i}$ shown in Fig. 5. The details will be presented in the following.

**Remark 4**: Note that the rotation matrix $\boldsymbol{R}_b^{wi}$ here is not for a coordinate transformation. It is responsible for transforming the wind-induced forces, i.e., the drag force and the lift force, to the body-fixed frame $\{B\}$. The superscript $wi$ here is another coordinate used to express the lift force and drag force. Because it only appears once, the formal definition is omitted to keep the paper clear and short.

### 5.1.2. Angular updating rate

The matrix $\boldsymbol{T}(\boldsymbol{\Theta}_{bn})$ transforms the body-fixed angular velocity to the Euler angle update rate, given by

$$
\boldsymbol{T}(\boldsymbol{\Theta}_{bn})^{-1}\dot{\boldsymbol{\Theta}}_{bn} = \begin{bmatrix} 0 \\ \dot\theta \\ 0 \end{bmatrix} + \boldsymbol{R}_{y,\theta}^\top \begin{bmatrix} \dot\phi \\ 0 \\ 0 \end{bmatrix} + \boldsymbol{R}_{y,\theta}^\top \boldsymbol{R}_{x,\phi}^\top \begin{bmatrix} 0 \\ 0 \\ \dot\psi \end{bmatrix}.
\tag{21}
$$

Removing $\dot{\boldsymbol{\Theta}}_{bn}$ from both sides yields

$$
\boldsymbol{T}(\boldsymbol{\Theta}_{bn})^{-1} = \begin{bmatrix} c\theta & 0 & -c\phi s\theta \\ 0 & 1 & s\phi \\ s\theta & 0 & c\phi c\theta \end{bmatrix}.
\tag{22}
$$

Hence,

$$
\boldsymbol{T}(\boldsymbol{\Theta}_{bn}) = \begin{bmatrix} c\theta & 0 & s\theta \\ t\phi s\theta & 1 & -c\theta t\phi \\ -s\theta/c\phi & 0 & c\theta/c\phi \end{bmatrix}.
\tag{23}
$$

**Remark 5**: Note that this update law will cause drift because $\boldsymbol{T}(\boldsymbol{\Theta}_{bn})$ is only a first-order approximation [30]. However, the drift is small with restoring forces acting on the payload. Hence, this simplification is suitable for control design.

### 5.2. Blade kinetics

A turbine blade is free to move in 6 DOFs. Assume that the yoke and the blade are rigidly fixed to each other. The yoke COG coincides with the blade COG as a single body. We disregard the moment of inertia of the yoke, while the air resistance is included in the relative motion of the wind load. The overall kinetics of the blade and yoke in $\{B\}$ about its COG is given by

$$
\boldsymbol{M}_b\dot{\boldsymbol{\nu}}_b + \boldsymbol{C}_b(\boldsymbol{\nu}_b)\boldsymbol{\nu}_b = \boldsymbol{g}_b^b + \boldsymbol{\tau}_s^b + \boldsymbol{\tau}_t^b + \boldsymbol{\tau}_w^b,
\tag{24}
$$

where $\boldsymbol{g}_b^b \in \mathbb{R}^6$ is the gravity force and moment vector in $\{B\}$, i.e.,

$$
\boldsymbol{g}_b^b = \begin{bmatrix} \boldsymbol{R}_b^{n\top}[0,0,(m_b+m_y)g]^\top \\ [0,0,0]^\top \end{bmatrix},
\tag{25}
$$

$\boldsymbol{\tau}_s^b$, $\boldsymbol{\tau}_t^b$, and $\boldsymbol{\tau}_w^b \in \mathbb{R}^6$ are the external load vectors from slings and tugger lines and wind-induced loads in $\{B\}$, i.e.,

$$\boldsymbol{\tau}_s^b = \sum_{i=1}^{n_s} \begin{bmatrix} \boldsymbol{R}_b^{n\top} \boldsymbol{f}_{si_B} \\ \boldsymbol{S}(\boldsymbol{p}_{si}^b - \boldsymbol{p}_{COG}^b)\boldsymbol{R}_b^{n\top} \boldsymbol{f}_{si_B} \end{bmatrix}, \tag{26}$$

$$\boldsymbol{\tau}_t^b = \sum_{i=1}^{n_t} \begin{bmatrix} \boldsymbol{R}_b^{n\top} \boldsymbol{f}_{ti_B} \\ \boldsymbol{S}(\boldsymbol{p}_{ti}^b - \boldsymbol{p}_{COG}^b)\boldsymbol{R}_b^{n\top} \boldsymbol{f}_{ti_B} \end{bmatrix}, \tag{27}$$

where $\boldsymbol{p}_{si}^b$ and $\boldsymbol{p}_{ti}^b$ are the positions of the connecting points of the slings and tugger lines, respectively. The mass matrix is

$$\boldsymbol{M}_b = \begin{bmatrix} (m_b + m_y)\boldsymbol{I}_3 & \boldsymbol{0}_3 \\ \boldsymbol{0}_3 & \boldsymbol{I}_b \end{bmatrix}, \tag{28}$$

where $m_b$ is the mass of the blade, $m_y$ is the mass of the yoke, and $\boldsymbol{I}_b \in \mathbb{R}^{3\times 3}$ is the inertia matrix. The mass of the blade $m_b$ is given by

$$m_b = \sum_{i=0}^{n} m_{bi} = \sum_{i=0}^{n} \rho_{bi}\Delta l_{bi}, \tag{29}$$

where $\rho_{bi}$ is the mass per unit length at the $i^{th}$ node,

$$\Delta l_{bi} = \begin{cases} \frac{1}{2}(r_{b,1} - r_{b,0}), & i = 0, \\ \frac{1}{2}(r_{b,i+1} - r_{b,i-1}), & i = 1, \cdots, n-1, \\ \frac{1}{2}(r_{b,n} - r_{b,n-1}), & i = n. \end{cases} \tag{30}$$

in which $r_{b,i}$ with $i = 0, \cdots, n$ denotes the axial distance from the position of the $i^{th}$ node to the blade root center.

For a vector $\boldsymbol{\lambda} = [\lambda_1, \lambda_2, \lambda_3]^\top \in \mathbb{R}^3$, the matrix $\boldsymbol{S}(\boldsymbol{\lambda})$ [29] in Eqns. (26)-(27) is given by

$$\boldsymbol{S}(\boldsymbol{\lambda}) = \begin{bmatrix} 0 & -\lambda_3 & \lambda_2 \\ \lambda_3 & 0 & -\lambda_1 \\ -\lambda_2 & \lambda_1 & 0 \end{bmatrix}. \tag{31}$$

The Coriolis matrix [29] then becomes

$$\boldsymbol{C}_b = -\boldsymbol{C}_b^\top = \begin{bmatrix} (m_b + m_y)\boldsymbol{S}(\boldsymbol{\omega}_b) & \boldsymbol{0}_3 \\ \boldsymbol{0}_3 & -\boldsymbol{S}(\boldsymbol{I}_b\boldsymbol{\omega}_b) \end{bmatrix}. \tag{32}$$

The blade dynamics is implemented in the MarIn module called `Payload/Suspended blade`.

## 5.3. Wind field

Unlike an operational turbine, the wind-induced motion to the different sections of the blade is small. When calculating the aerodynamic loads, the blade is assumed to be divided into a group of $n$ small segments with $n+1$ nodes, enumerated from 0 to $n$. The total wind-induced load to the blade is basically the integration of local two-dimensional elemental loads acting along the span according to the cross-flow principle.

During a single blade installation, the wind-induced loads are the main external disturbance. Because the lengths of the blade are often greater than 60 m for a 5 MW turbine, a time-varying wind velocity should be considered. The wind load limits the weather window; therefore, uniform wind is not sufficient to calculate the wind-induced load in this case. The wind velocity at a point in space $(x, y, z)$ at time $t$, denoted by $\boldsymbol{v}_w(x, y, z, t)$, is the sum of the mean wind speed and the turbulence, i.e.,

$$\boldsymbol{v}_w(x, y, z, t) = \bar{\boldsymbol{v}}_w(\boldsymbol{R}_w^n, t) + \boldsymbol{v}_{TI}(x, y, z, t), \tag{33}$$

where $\bar{\boldsymbol{v}}_w(t) = \boldsymbol{R}_w^n[U_w(t), 0, 0]^\top$ is the mean wind velocity vector in $\{N\}$, $U_w$ is the mean wind speed, and $\boldsymbol{v}_{TI}(x, y, z, t)$ is the spatio-temporal turbulence velocity at $(x, y, z)$.

### 5.3.1. Wind turbulence

The Taylor's hypothesis of frozen turbulence is adopted and assumes that the advection of a field of turbulence past a fixed point can be taken to be entirely due to the mean flow, as the contribution from the turbulent circulation is small. This only holds if the relative turbulence intensity ($TI$) is small, that is, $\frac{U_e}{U_w} \ll 1$, where $U_e$ refers to the eddy velocity.

A turbine box is assumed in a space with evenly distributed points inside that moves with the mean wind speed $U_w$ in the length direction, i.e., $x^w$-axis. The size of the turbulence box is $N_{wx} \times N_{wy} \times N_{wz}$ with intervals $D_{wx}$, $D_{wy}$, and

$D_{wz}$ along the corresponding axes, where $N_{wx}$, $N_{wy}$, and $N_{wz}$ are the numbers of points in the $x^w$-, $y^w$-, and $z^w$-axes, respectively [31]. The wind turbulence boxes are generated by importing and reshaping the binary files from TurbSim [32, 33], with preset discrete points along the length, width, and height. TurbSim is a free stochastic turbulence simulator [34]. Additionally, the binary turbulence file generated by HAWC2 is also supported. According to a rule of thumb in aeroelastic simulations, the grid sizes are chosen to be smaller than the blade root diameter in order to capture the effects of wind speed variation of the turbulent wind field on the blade loads.

A blade is a smooth interpolation of a number of cross sections. The position of a point in $\{N\}$ is transformed to the position in $\{W\}$. To remain consistent, the wind force is considered to act on the center of pressure $C_{1/4}$ based on the wind velocity at $C_{1/4}$. The position of $C_{1/4}$ at the $i^{th}$ cross section in $\{N\}$ is defined by $\boldsymbol{p}_{C_{1/4},i} = [x_{C_{1/4},i}, y_{C_{1/4},i}, z_{C_{1/4},i}]^\top$. The wind velocity vector at the $i^{th}$ node in $\{N\}$, $\boldsymbol{v}_{wi}(\boldsymbol{p}_{C_{1/4},i}, t) = [u_{wi}, v_{wi}, w_{wi}]^\top$, is interpolated by a 3D lookup table with the following relation:

$$\boldsymbol{v}_{wi} = \boldsymbol{R}_w^n \left( \begin{bmatrix} U_w \\ 0 \\ 0 \end{bmatrix} + \begin{bmatrix} \boldsymbol{\Omega}_{x,mann}^w(\boldsymbol{p}_{C_{1/4},i}^w, t) \\ \boldsymbol{\Omega}_{y,mann}^w(\boldsymbol{p}_{C_{1/4},i}^w, t) \\ \boldsymbol{\Omega}_{z,mann}^w(\boldsymbol{p}_{C_{1/4},i}^w, t) \end{bmatrix} \right) \tag{34}$$

with

$$\boldsymbol{p}_{C_{1/4},i}^w = \begin{bmatrix} x_{C_{1/4},i}(t) + \int_0^t U_w(\tau)d\tau - x_{O_w} \\ y_{C_{1/4},i}(t) - y_{O_w} \\ z_{C_{1/4},i}(t) - z_{O_w} \end{bmatrix}, \tag{35}$$

where $\boldsymbol{\Omega}_{x,mann}^w$, $\boldsymbol{\Omega}_{y,mann}^w$, and $\boldsymbol{\Omega}_{z,mann}^w$ are the generated turbulence boxes for the $x^w$-, $y^w$-, and $z^w$-directions, respectively.

This turbulence is implemented in the MarIn module called `Environment/3D wind generator with turbulence`.

### 5.3.2. Wind-induced loads acting on a blade

A centerline is defined in the main-body coordinate system. Because the NREL 5 MW reference wind turbine blade does not have a prebend, the centerline is almost a straight line. The aerodynamic center $C^1/_2$ of a cross section lays on the centerline with a rotation $\theta_{y,i}$ about the $y^b$-axis in the main-body $x^b$-$z^b$ coordinate plane. The centerline connects all $C^1/_2$ from the blade root to the blade tip. The root is defined using a circular shape. The shape of the main blade body is a series of airfoils with various chord lengths, geometric centers, and thickness/chord ratios (T/C). Define $T/C_i = \frac{t_i}{C_i}$, where $C_i$ and $t_i$ are the chord length and the maximum thickness of the $i^{th}$ airfoil section. In a quasi-steady analysis, the aerodynamic coefficients are a function of the AOA and T/C. The structural parameters and aerodynamic coefficients can be obtained by interpolation though data from the reference turbine. The aerodynamic load calculation is based on the following assumptions:

- Rigid structure: blade vibration is negligible.

- Vertex shedding or dynamic stall can be ignored.

The lift force, drag force, and pitching moment acting on the $i^{th}$ node, denoted by $L_i$, $D_i$, and $M_i$, are calculated with airfoil theory [35] and an integration along the span. This gives

$$L_i = \frac{1}{2}\rho_a C_l(\alpha_i, T/C_i)A_i V_i^2, \tag{36}$$

$$D_i = \frac{1}{2}\rho_a C_d(\alpha_i, T/C_i)A_i V_i^2, \tag{37}$$

$$M_i = \frac{1}{2}\rho_a C_m(\alpha_i, T/C_i)A_i V_i^2, \tag{38}$$

where the subscript $i$ refers to the $i^{th}$ node, $\rho_a$ is the air density, and $C_l$, $C_d$, and $C_m$ denote the lifting coefficient, the drag coefficient, and the pitching moment coefficient, respectively. The inflow speed is $V_i = |\boldsymbol{L}[\boldsymbol{R}_n^{bi}(\boldsymbol{v}_{wi} - \boldsymbol{v}_{C_{1/4},i})]|$, where $\boldsymbol{L} = \begin{bmatrix} 1 & 0 & 0 \\ 0 & 0 & 1 \end{bmatrix}$, and $\boldsymbol{v}_{C_{1/4},i}$ are the velocity vector of the $i^{th}$ center of pressure in $\{N\}$, respectively. Note that the relative velocity here contributes to the air resistance. The wing area is

$$A_i = \begin{cases} \frac{(r_{b,1}-r_{b,0})C_1}{2} & \text{if } i = 0, \\ \frac{(r_{b,i}-r_{b,n-1})C_n}{2} & \text{if } i = n, \\ \frac{(r_{b,i}-r_{b,i-1})C_i}{2} + \frac{(r_{b,i+1}-r_{b,i})C_{i+1}}{2} & \text{otherwise.} \end{cases} \tag{39}$$

The AOA at the $i^{th}$ segment $\alpha_i$ is given by

$$\alpha_i = \alpha + \theta_{y,i}, \tag{40}$$

with

$$\alpha = f_a\big(\pi + \operatorname{atan2}(w_{wi}^b - w_{C_{1/4}}^b, u_{wi}^b - u_{C_{1/4}}^b)\big), \tag{41}$$

where $f_a$ is a function that converts an angle to the range $[-\pi, \pi)$, $\operatorname{atan2}(y, x)$ is the multi-valued inverse tangent function, and $w_{wi}^b - w_{C_{1/4}}^b$ and $u_{wi}^b - u_{C_{1/4}}^b$ denote the relative wind velocity at the $i^{th}$ blade segment center in $\{B\}$. For small $\alpha_i$ in the range [-45,45] deg, a series of aerodynamic coefficients w.r.t. the AOA has been calculated and stored in a lookup table. For high $\alpha_i$, in the ranges [-180,-45] and [45,180] deg, the aerodynamic coefficients are calculated as flat plates, which are given by

$$C_l(\alpha_i, \mathrm{T/C}_i) = 2\cos(\alpha_i)\sin(\alpha_i), \tag{42a}$$

$$C_d(\alpha_i, \mathrm{T/C}_i) = \overline{C}_d(\mathrm{T/C}_i)\sin^2(\alpha_i), \tag{42b}$$

$$C_m(\alpha_i, \mathrm{T/C}_i) = -\sin(\alpha_i)/4, \tag{42c}$$

where $\overline{C}_d(\mathrm{T/C})$ is the maximum value for $C_d$ with respect to T/C [36]. The coefficients for an arbitrary AOA are then found by interpolation.

When the yaw angle is small, the force component in the $y^b$-axis is negligible according to the cross-flow principle. Consequently, the resulting force and moment vector acting at the $i^{th}$ node in the blade main-body frame $\{B\}$ are given by

$$\boldsymbol{f}_{w,i}^b = \boldsymbol{R}_b^{wi\top} \begin{bmatrix} -D_i \\ 0 \\ L_i \end{bmatrix}, \tag{43}$$

$$\boldsymbol{m}_{w,i}^b = \boldsymbol{m}_{w,i}^{wi} = \begin{bmatrix} 0 \\ M_i \\ 0 \end{bmatrix}. \tag{44}$$

Therefore, the total wind-induced force and moment acting on the main-body COG are given by

$$\boldsymbol{\tau}_w^b = \begin{bmatrix} \sum_{i=0}^n \boldsymbol{f}_{w,i}^b \\ \sum_{i=0}^n \left[ \boldsymbol{S}(\boldsymbol{p}_{C_{1/4},i}^b - \boldsymbol{p}_{COG}^b)\boldsymbol{f}_{w,i}^b + \boldsymbol{m}_{w,i}^b \right] \end{bmatrix}. \tag{45}$$

These wind-induced loads are implemented in the MarIn module called `Payload/Wind-induced load acting on the blade`.

## 6. Code-to-code verification of the blade model with quasi-static analysis

In this section, a series of code-to-code verification tests are conducted to verify that the proposed code models the blade with realistic parameters and coefficients. The tests are conducted using the HAWC2 and MATLAB/Simulink with the NREL 5 MW reference wind turbine. The aerodynamic coefficients are read from the HAWC2 .dat file, to obtain the same wind loads and perform a fair comparison study. A brief summary of the blade is tabulated in Table 3. In the simulations of this section, the wind velocity is constant without turbulence. In the next section, we will introduce turbulence and conduct testing with more realistic wind loads.

### 6.1. Test 1. Mass and moment of inertia

The mass, the moment of inertia, and the COG position are calculated by a user-defined function `init_blade_hawc2`. The function reads the structural coefficients from HAWC2 files. This test attempts to verify that the function `init_blade_hawc2` reads the correct parameters from the HAWC2 data files and calculates the correct mass matrix and COG position. The results are tabulated in Table. 4. From the results, the `init_blade_hawc2` function outputs are close to those from HAWC2.

Table 3: Basic parameters of a single blade installation configuration with the NREL 5 MW turbine blade.

| Parameter | Symbol | Unit | Value |
|---|---|---|---|
| Mass of blade | $m_b$ | ton | 17.74 |
| Length of blade | $l_b$ | m | 61.5 |
| Mass of yoke | $m_y$ | ton | 20 |
| Mass of hook | $m_h$ | ton | 1 |
| Length of lift wire 1 | $l_l$ | m | 10 |
| Stiffness of lift wire 1 | $k_l$ | N/m | 1e8 |
| Damping of lift wire 1 | $d_l$ | N·m/s | 1e4 |
| Length of sling 1 | $l_{s1}$ | m | 9.2 |
| Stiffness of sling 1 | $k_{s1}$ | k/m | 1e8 |
| Damping of sling 1 | $d_{s1}$ | N·m/s | 1e4 |
| Length of sling 2 | $l_{s2}$ | m | 9.2 |
| Stiffness of sling 2 | $k_{s2}$ | N/m | 1e8 |
| Damping of sling 2 | $d_{s2}$ | N·m/s | 1e8 |
| Length of tugger line 1 | $l_{t1}$ | m | 9.17 |
| Stiffness of tugger line 1 | $k_{t1}$ | k/m | 1e7 |
| Damping of tugger line 1 | $d_{t1}$ | N·m/s | 0 |
| Length of tugger line 2 | $l_{t2}$ | m | 9.17 |
| Stiffness of tugger line 2 | $k_{t2}$ | N/m | 1e7 |
| Damping of tugger line 2 | $d_{t2}$ | N·m/s | 0 |
| Size of the turbulence box | $N_{wx}, N_{wy}, N_{wz}$ | - | 65536, 32, 16 |
| Intervals of the turbulence box | $D_{wx}, D_{wy}, D_{wz}$ | m | 4, 4, 4 |

## 6.2. Test 2. Aerodynamic-coefficient lookup tables

Due to the rotation of the centerline and axial-varying thickness, the aerodynamic coefficients along the blade span are also varied. The `init_blade_hawc2` function reads the aerodynamic coefficients to construct lookup tables for the aerodynamic force modules. For the NREL 5 MW reference turbine blade, the resulting aerodynamic coefficients w.r.t. blade AOA and T/C are shown in Figs. 7-9. The curves agree with the results in Ref. [25]. Therefore, the `init_blade_hawc2` function is accepted to correctly read the aerodynamic coefficients from the HAWC2 data files.

Table 4: Mass and moment of inertia verify the NREL 5 MW blade.

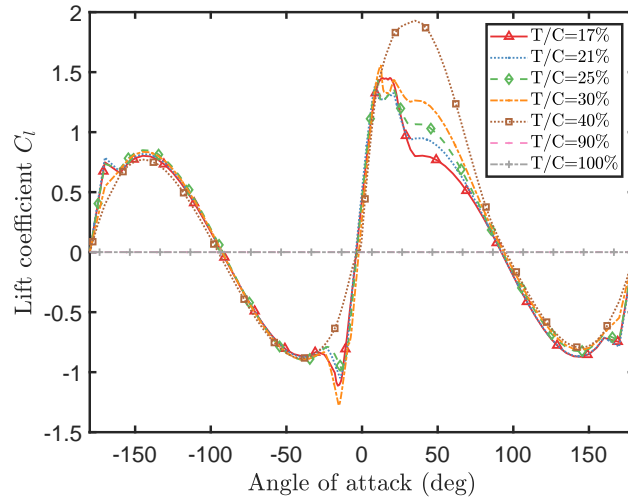| Parameters | HAWC2 outputs | Proposed user-defined function |
|---|---|---|
| Mass (kg) | 17704 | 17740 |
| Position of COG in $\{B\}$ (m) | $[0.145 \quad 0.022 \quad 20.561]$ | $[-0.1454 \quad 0.089 \quad 20.507]$ |
| Inertia at the root center in $\{B\}$ (kg·m$^2$) $[I_{xx}, I_{yy}, I_{zz}; I_{xy}I_{xz}, I_{yz}]$ | $\begin{bmatrix} 1.1808e7 & 2.6714e4 & 1.1817e7 \\ -6.556e4 & -1.417e3 & -7.166e3 \end{bmatrix}$ | $\begin{bmatrix} 1.1776e7 & 2.6837e4 & 1.1776e7 \\ -6.515e4 & -1.491e3 & -7.097e3 \end{bmatrix}$ |

Figure 7: $C_l$ lookup table w.r.t. airfoil thickness/chord ratio and AOA for the NREL 5 MW wind turbine blade.
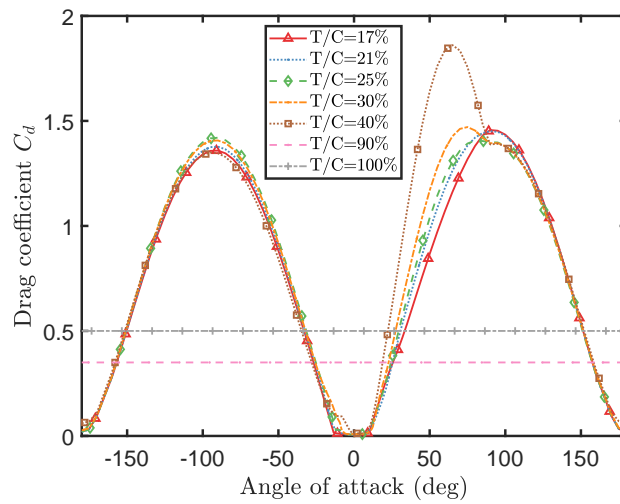


Figure 8: $C_d$ lookup table w.r.t. airfoil thickness/chord ratio and AOA for the NREL 5 MW wind turbine blade.
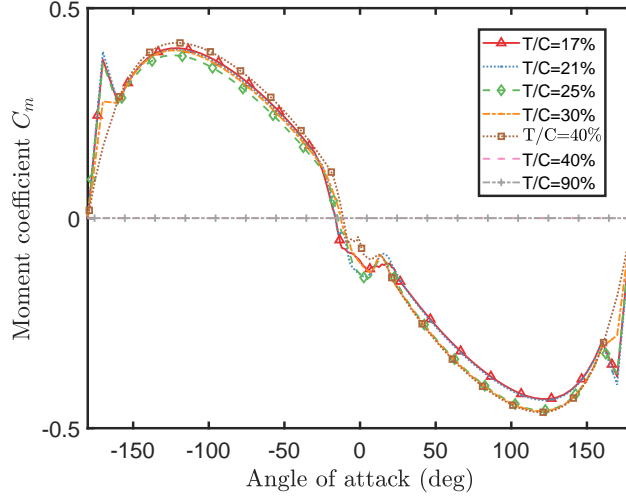
Figure 9: $C_m$ lookup table w.r.t. airfoil thickness/chord ratio and AOA for the NREL 5 MW wind turbine blade.

### 6.3. Test 3. Aerodynamic coefficients and force along the blade axis

We conducted tests to verify the wind-induced load acting on the blade with respect to different wind speeds, roll angles, and yaw angles, i.e., the algorithm proposed in Section 5.3.2. The blade is fixed at 90 m above the sea surface with $\psi = 0$ deg and $\psi = 30$ deg, respectively. The horizontal wind speed at the height of 90 m is 10 m/s in the global negative $x$-direction. The pitch angle is set to 10, 30, 50, 60, and 90 degrees. The wind speeds up during the first 20 seconds, and the results are the corresponding values at 100 seconds. For the HAWC2 model, the wind-induced load quadratically increases with a slight delay at the later stage. After the wind speed reaches a steady value, the wind-induced load is constant. The proposed model calculates the wind load quadratically according to the wind speed. The aerodynamic coefficients and forces are illustrated at various spanwise cross-planes as shown in Figs. 10-13. In the figures, curves from the HAWC2 and the proposed Simulink model agree well. Therefore, the results confirm that the Simulink module calculates the aerodynamic coefficients and force correctly.
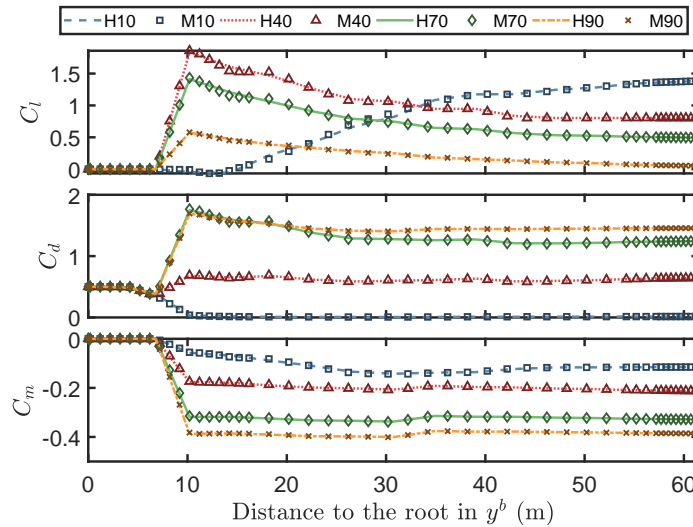


Figure 10: Aerodynamic coefficients $C_l$, $C_d$, $C_m$, $\psi = 0$ deg, w.r.t. $\theta$ and $y^b$. (In the legend, H and M denote the results from HAWC2 and the proposed toolbox, respectively. The numbers represent the pitch angles in deg.)
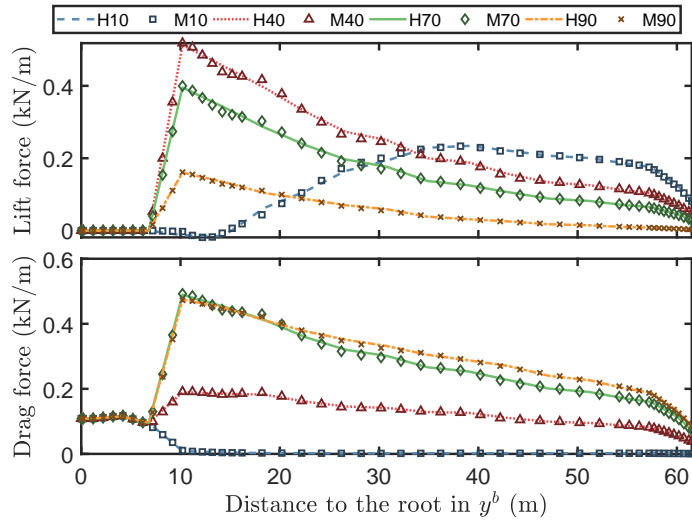
16

Figure 11: Lift force and drag force per unit length $\psi = 0$ deg, w.r.t. $\theta$ and $y^b$, wind speed = 10 m/s. (In the legend, H and M denote the results from HAWC2 and the proposed toolbox, respectively. The numbers represent the pitch angles in deg.)
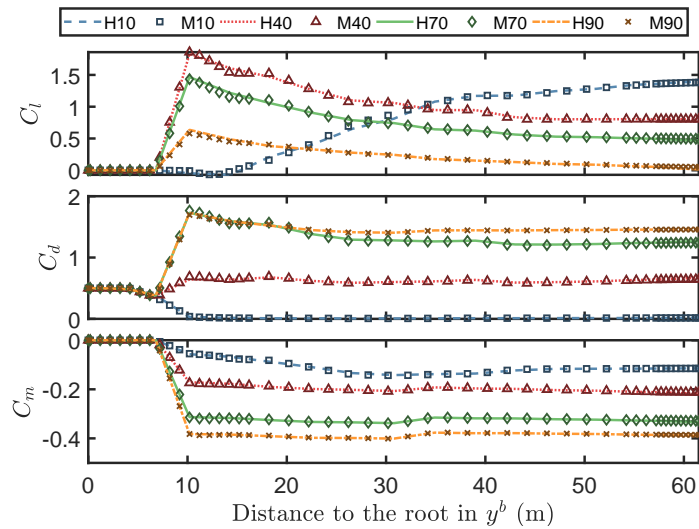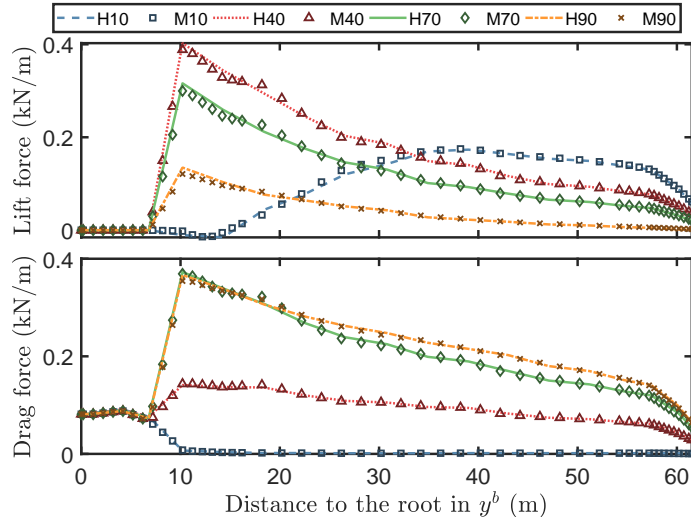


Figure 12: Aerodynamic coefficients, $\psi = 30$ deg, $C_l$, $C_d$, $C_m$ w.r.t. $\theta$ and $y^b$. (In the legend, H and M denote the results from HAWC2 and the proposed toolbox, respectively. The numbers represent the pitch angles in deg.)

Figure 13: Lift force and drag force per unit length, $\psi = 30$ deg, w.r.t. $\theta$ and $y^b$, wind speed $= 10$ m/s. (In the legend, H and M denote the results from HAWC2 and the proposed toolbox, respectively. The numbers represent the pitch angles in deg.)

## 6.4. Test 4. Total wind-induced load acting on the blade

The total load acting on the blade is tested with respect to various wind speeds and blade pitch angles. The wind speed is from 0 to 20 m/s with a 1 m/s interval. The pitch angle is from 10° to 90° with a 10 deg interval. The blade yaw is 0°, i.e., the wind loads are at their maxima in this situation. The resulting forces at the steady states are presented in Fig. 14. From the results, it is noticed that the wind-generated forces $F_x$ and $F_z$ are well-fitted and are proportional to the square of the mean wind speed. This observation corresponds well with [4]. Deviations between the HAWC2 and the proposed model occur in the subplot $F_y$. This is because of the different mechanics used in simulation, that is, Timoshenko beam elements in HAWC2 and the rigid body with assumed zero sway force in the proposed model. Comparing with the magnitudes of $F_x$ and $F_z$, the deviation in $F_y$ is very small and considered negligible for the intended use of our model.

The same issue appears in simulations with $\psi = 30°$, whose results are presented in Fig. 15.



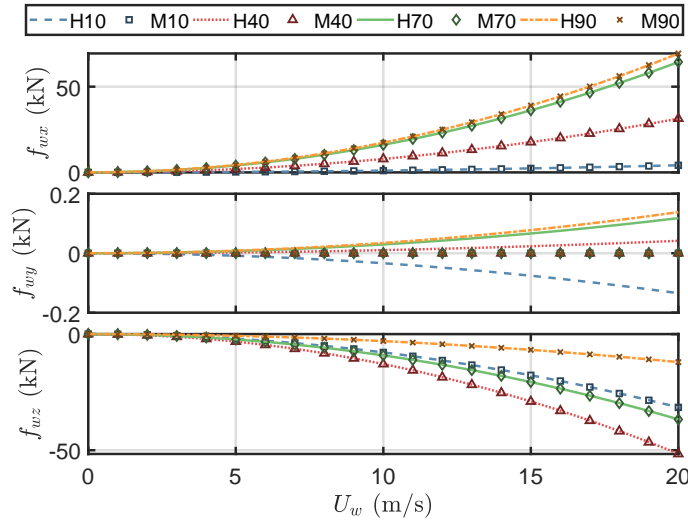Figure 14: Total force acting on the blade in $\{B\}$, $\psi = 0$ deg. (In the legend, H and M denote the results from HAWC2 and the proposed toolbox, respectively. The numbers represent the pitch angles in deg.)
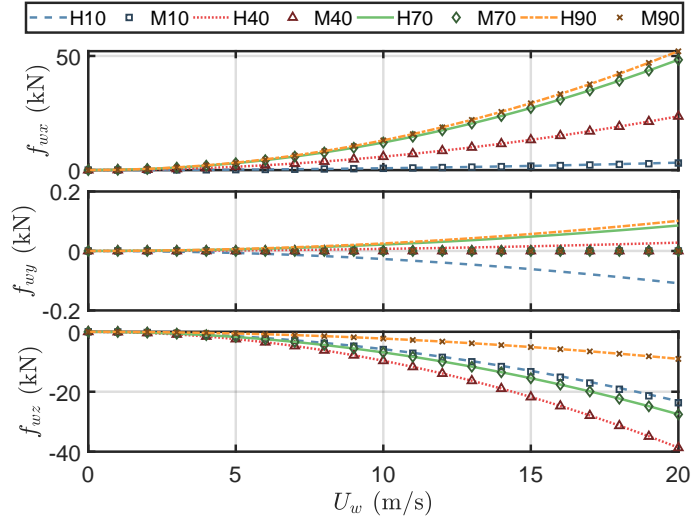
18

Figure 15: Total force acting on the blade in $\{B\}$, $\psi = 30$ deg. (In the legend, H and M denote the results from HAWC2 and the proposed toolbox, respectively. The numbers represent the pitch angles in deg.)

## 7. Case study: single blade installation model

After confirming the performance of each module individually, the overall single blade installation model is built. A single blade installation is performed with a yoke that grabs and holds the blade around the center of gravity. The yoke is lifted by lift wires from a crane and stabilized by tugger lines symmetrically arranged around the COG on the blade axis.

The model is, to a certain degree, of low fidelity due to the lack of complex aerodynamic effects. This increases the run-time performance of the model while maintaining the most important dynamic effects for the purposes of control design and analysis.

### 7.1. Modeling procedure

All modules and basic functions are packaged as an individual package of MarIn toolbox, which will be integrated into MarIn in the future; see Fig. 16. The single blade installation model, presented in Figs. B.22-B.23, is given as an example of the use of this toolbox. Newton-Euler mechanics is used to connect the modules in the inflow direction.
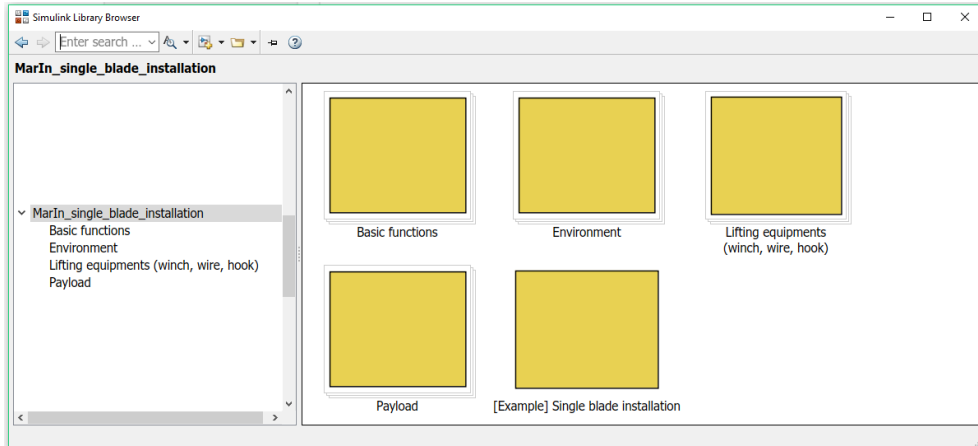


Figure 16: Interface of the toolbox in Simulink library browser.

### 7.2. Test 5. Equilibrium point in steady wind

First, tests concerning the equilibrium points in an environment with constant wind speed are conducted. For the nonrotating blade studied under a constant wind speed, the displacements of the root center, the COG, and the tip center

19

around their equilibrium positions approximately follow a quadratic relation with the wind speed. This observation is aligned with [4, 20]. The position of the crane and the lengths of all the wire ropes are fixed. The blade leading edge is downward, i.e., the pitch angle is equal to -90°and $\mathbf{\Theta}_{bn}(0) = [0, -\pi/2, 0]^\top$. The mean wind direction is in the x-axis, i.e., $\mathbf{\Theta}_{wn} = [0, 0, 0]^\top$.

A constant wind speed starts acting on the blade with a 5-second ramp increasing. The results are presented in Figs. 17 and 18. The displacements of the root center, COG, and tip center all satisfy quadratic relations.
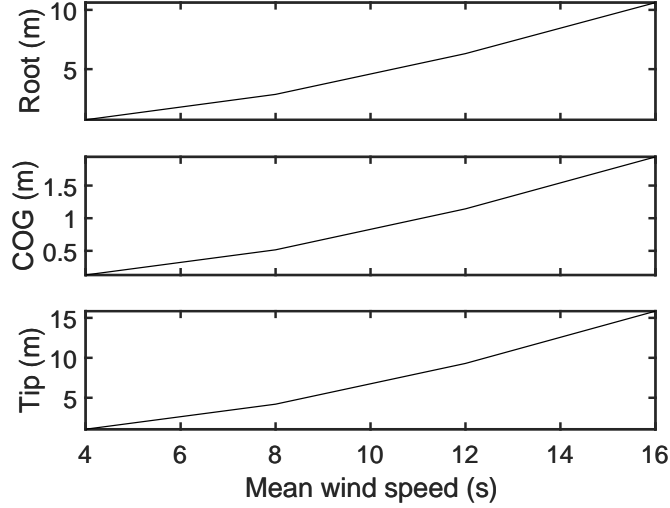


Figure 17: Displacements of the equilibrium point of the root center, the tip center, and the COG, under various mean wind speeds without turbulence.
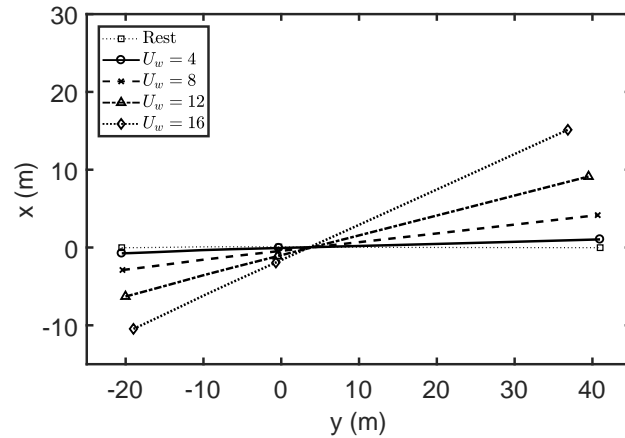


Figure 18: Equilibrium positions of the blade centerline in the x-y horizontal plane under constant mean wind speeds without turbulence.

### 7.3. Test 6. Time-domain simulation with wind turbulence

In practical situations, the wind speed is not constant. Therefore, a complex turbulent wind field is used in the simulation. The external loads are caused by the wind field with spatio-temporal turbulence; see Ref. [20] for more details. The mean wind speed is set to 12 m/s, and $TI = 0.146$. The seed number is set to 94.

The simulations are conducted with a personal computer with an Intel Core i7 3.6 GHz CPU using MATLAB version R2017b. The solver in Simulink is more powerful and flexible than aerodynamic software. A variable step size and the maximum step size can be set to ensure both accuracy and efficiency. For a 1000-second simulation, the average

20

computation time is 710 seconds. Therefore, the proposed simulation model is fast enough for the simulation. The histories of the blade root position, COG position, and tip position are presented in Figs. 19-21. As shown, the motions in the x-direction are dominant, and the pendulum mode (0.1 Hz) of the blade system is visible in the time series of the blade root. Under the turbulent wind condition, the blade root and the blade tip experience significantly larger motions compared to the blade COG. For the blade root, the displacement 553.6 % increase in x, 152.0 %increase in y, 2482.2 % increase in z. The motion at the blade tip is even larger, whose displacement 823.3 % increase in x, 303.1 %increase in y, 4701.1 % increase in z.
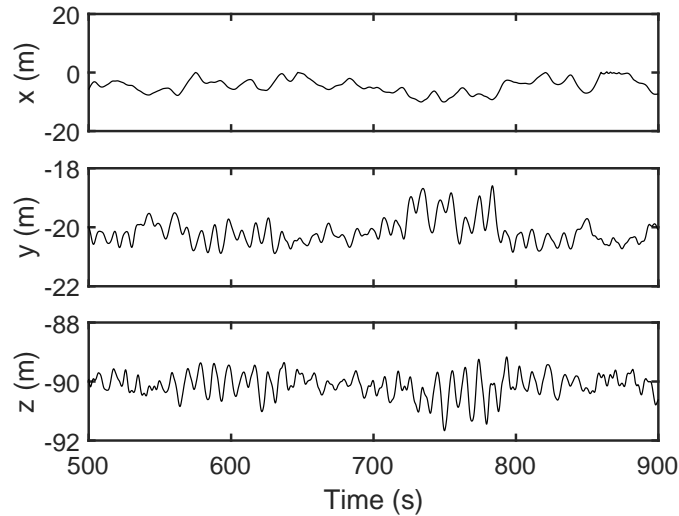


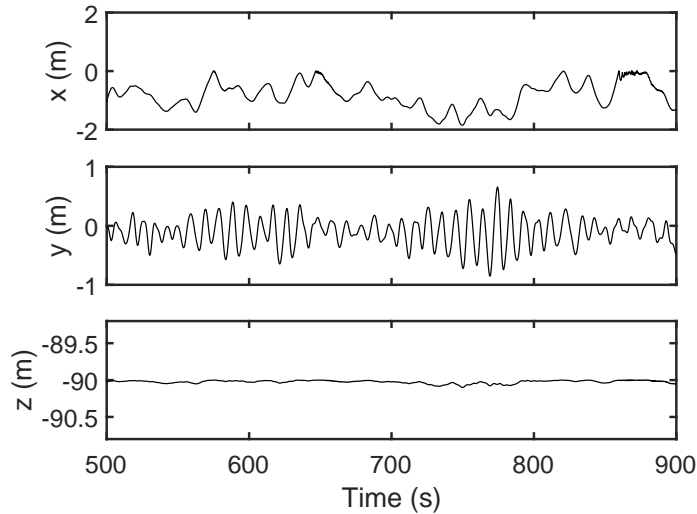Figure 19: Position of the blade root center, $U_w = 12$ m/s, $TI = 0.146$.



Figure 20: Position of the blade COG, $U_w = 12$ m/s, $TI = 0.146$.

## 8. Conclusion and future research

In this paper, a numerical modeling framework for blade installation for wind turbine is presented. A single blade installation model is given along with an example. The model is based on the Newton-Euler method. The hook, blade, lift wire, sling, tugger line, winch, and wind are modeled. Code-to-code verification studies are conducted to prove the effectiveness and correctness of the proposed model. This model presents a starting point for future research on OWT installation and related control and monitoring functions.
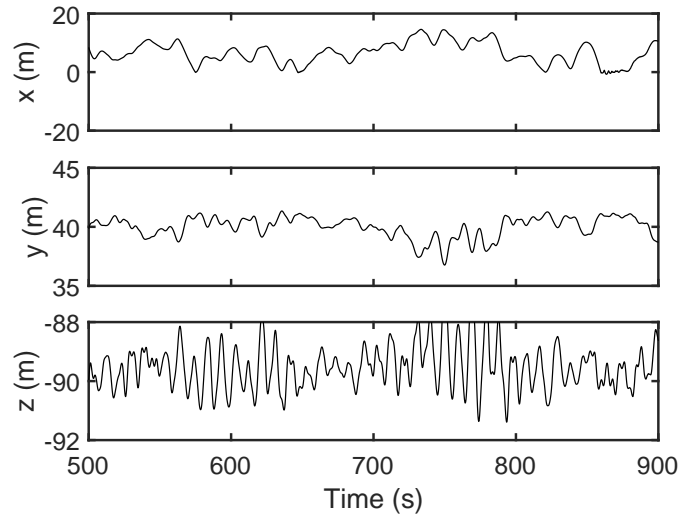
Figure 21: Position of the blade tip center, $U_w = 12$ m/s, $TI = 0.146$.

The model will be integrated with other modules to verify controllers for various scenarios of single blade installation as well as other marine operations with emphasis on crane operation. In the future, a structured and more comprehensive MarIn toolbox will be proposed specifically for marine operations.

# Appendix A. The I/O and parameter description

Table A.5: I/O and important parameters for the winch module.

| Module name | Winch | Symbol | Dimension |
|---|---|---|---|
| **Inputs** | Wire length changing rate (m/s) | $\dot{l}_1$ | [1] |
| **Outputs** | Wire length (m) | $l_1$ | [1] |
| **Parameters** | Initial wire length (m) | $l_1(0)$ | [1] |

Table A.6: I/O and important parameters for the wire rope module.

| Module name | Wire rope | Symbol | Dimension |
|---|---|---|---|
| **Inputs** | Positions of both ends (m) | $\boldsymbol{p}_A, \boldsymbol{p}_B$ | $[3 \times 1]$ |
|  | Wire length (m) | $l_1$ | [1] |
|  | Wire length changing rate (m/s) | $\dot{l}_1$ | [1] |
| **Outputs** | Forces at both ends (N) | $\boldsymbol{f}_A, \boldsymbol{f}_B$ | $[3 \times 1]$ |
| **Parameters** | Wire stiffness (N/s) | $d_r$ | [1] |
|  | Wire damping (N·s/m) | $k_r$ | [1] |

Table A.7: I/O and important parameters for the hook module.

| Module name | Hook | Symbol | Dimension |
|---|---|---|---|
| **Inputs** | Force input from the connected wires (N) | $\boldsymbol{f}_{li_B}, \boldsymbol{f}_{si_A}$ | $[3 \times 1]$ |
| **Outputs** | Position of the hook (m) | $\boldsymbol{p}_h$ | $[3 \times 1]$ |
| **Parameters** | Initial position of the hook(m) | $\boldsymbol{p}_h(0)$ | $[3 \times 1]$ |
|  | Initial velocity of the hook(m) | $\boldsymbol{v}_h(0)$ | $[3 \times 1]$ |
|  | Hook mass (kg) | $m_h$ | [1] |

Table A.8: I/O and important parameters for the wind generator module.

| Module name | 3D wind generator with turbulence | Symbol | Dimension |
|---|---|---|---|
| **Inputs** | Mean wind speed (m/s) | $U_w$ | [1] |
|  | Position of the given point(m) | $\boldsymbol{p}_{C_{1/4},i}$ | $[3 \times n]$ |
| **Outputs** | Wind velocity at the given points (m/s) | $\boldsymbol{\nu}_{wi}$ | $[3 \times n]$ |
| **Parameters** | Position of the turbulence box center (m) | $\boldsymbol{p}_{O_w}$ | [3] |
|  | Orientations of the turbulence box (rad) | $\boldsymbol{\Theta}_{wn}$ | [3] |
|  | Turbulence data structure | - | structure |

Table A.9: I/O and important parameters for the wind-induce loads.

| Module name | Wind-induced loads | Symbol | Dimension |
|---|---|---|---|
| **Inputs** | Position and orientations of the blade(m,rad) | $\boldsymbol{\eta}_b$ | [6] |
|  | Wind velocity at the centers of pressure of the airfoil segments (m/s) | $\boldsymbol{\nu}_{wi}$ | $[3 \times n]$ |
|  | Velocity at the centers of pressure of the airfoil segments (m/s) | $\boldsymbol{v}_{C_{1/4}}$ | $[3 \times n]$ |
| **Outputs** | Wind-induced load in the body-fixed frame (N,N·m) | $\boldsymbol{\tau}_w^b$ | [6] |
| **Parameters** | Blade aerodynamic coefficient structure | - | - |

Table A.10: I/O and important parameters for the suspended blade module.

| Module name | Suspended blade | Symbol | Dimension |
|---|---|---|---|
| **Inputs** | Force input from the connected wires (N) | $\boldsymbol{f}_{si_B}, \boldsymbol{f}_{ti_B}$ | $[3 \times n]$ |
| | Wind-induced load (N,N·m) | $\boldsymbol{\tau}_w^b$ | $[6]$ |
| **Outputs** | Position and orientations of the blade (m,rad) | $\boldsymbol{\eta}_b$ | $[6]$ |
| | Position of the positions of the connecting points of the connected wires (m) | $\boldsymbol{p}_{si}, \boldsymbol{p}_{ti}$ | $[3 \times n_s], [3 \times n_t]$ |
| | Position of the centers of pressure of the airfoil segments (m) | $\boldsymbol{p}_{C_{1/4},i}$ | $[3 \times n]$ |
| | Position of the blade aerodynamic centers (m) | $\boldsymbol{p}_{C_{1/2},i}$ | |
| **Parameters** | Initial position and velocity of the blade | $\boldsymbol{\eta}_b(0)$ | $[6]$ |
| | Yoke mass | $m_y$ | $[1]$ |
| | Blade data structure | - | - |
| | Positions of the connected points to the slings and tugger lines in $\{B\}$ | $\boldsymbol{p}_{si}^b, \boldsymbol{p}_{ti}^b$ | $[3 \times n_s], [3 \times n_t]$ |

## Appendix B. Modeling of single blade installation in Simulink

The blue labels in Figures B.22-B.23 are the section numbers in which the specific modules use equations.

[1] C. Moné, M. Hand, M. Bolinger, J. Rand, D. Heimiller, J. Ho, 2015 cost of wind energy review, Tech. rep., National Renewable Energy Laboratory (2017).

[2] M. J. Kaiser, B. Snyder, Offshore wind energy installation and decommissioning cost estimation in the US outer continental shelf, US Bureau of Ocean Energy Management, Enforcement and Regulation.

[3] Y. Zhao, Z. Cheng, P. C. Sandvik, Z. Gao, T. Moan, An integrated dynamic analysis method for simulating installation of single blades for wind turbines, Ocean Engineering 152 (2018) 72 – 88. doi:https://doi.org/10.1016/j.oceaneng.2018.01.046.

[4] M. Gaunaa, L. Bergami, S. Guntur, F. Zahle, First-order aerodynamic and aeroelastic behavior of a single-blade installation setup, in: Journal of Physics: Conference Series, Vol. 524, IOP Publishing, 2014, p. 012073.

[5] T. A. Johansen, T. I. Fossen, S. I. Sagatun, F. G. Nielsen, Wave synchronizing crane control during water entry in offshore moonpool operations-experimental results, IEEE Journal of Oceanic Engineering 28 (4) (2003) 720–728.

[6] Y. Fang, P. Wang, N. Sun, Y. Zhang, Dynamics analysis and nonlinear control of an offshore boom crane, IEEE Transactions on Industrial Electronics 61 (1) (2014) 414–427.

[7] B. Skaare, O. Egeland, Parallel force/position crane control in marine operations, IEEE Journal of Oceanic Engineering 31 (3) (2006) 599–613.

[8] Z. Ren, Z. Jiang, R. Skjetne, Z. Gao, Active tugger line force control for single blade installation, Wind EnergyUnder review.

[9] P. Wang, X. Tian, T. Peng, Y. Luo, A review of the state-of-the-art developments in the field monitoring of offshore structures, Ocean Engineering 147 (2018) 148–164.

[10] X. Tian, P. Wang, X. Li, X. Wu, W. Lu, C. Wu, Z. Hu, H. Rong, H. Sun, A. Wang, et al., Design and application of a monitoring system for the floatover installation, Ocean Engineering 150 (2018) 194–208.

[11] T. Perez, Ø. N. Smogeli, T. I. Fossen, A. J. Sørensen, An overview of the marine systems simulator (MSS): A simulink® toolbox for marine control systems, Modeling, identification and Control 27 (4) (2006) 259–275.
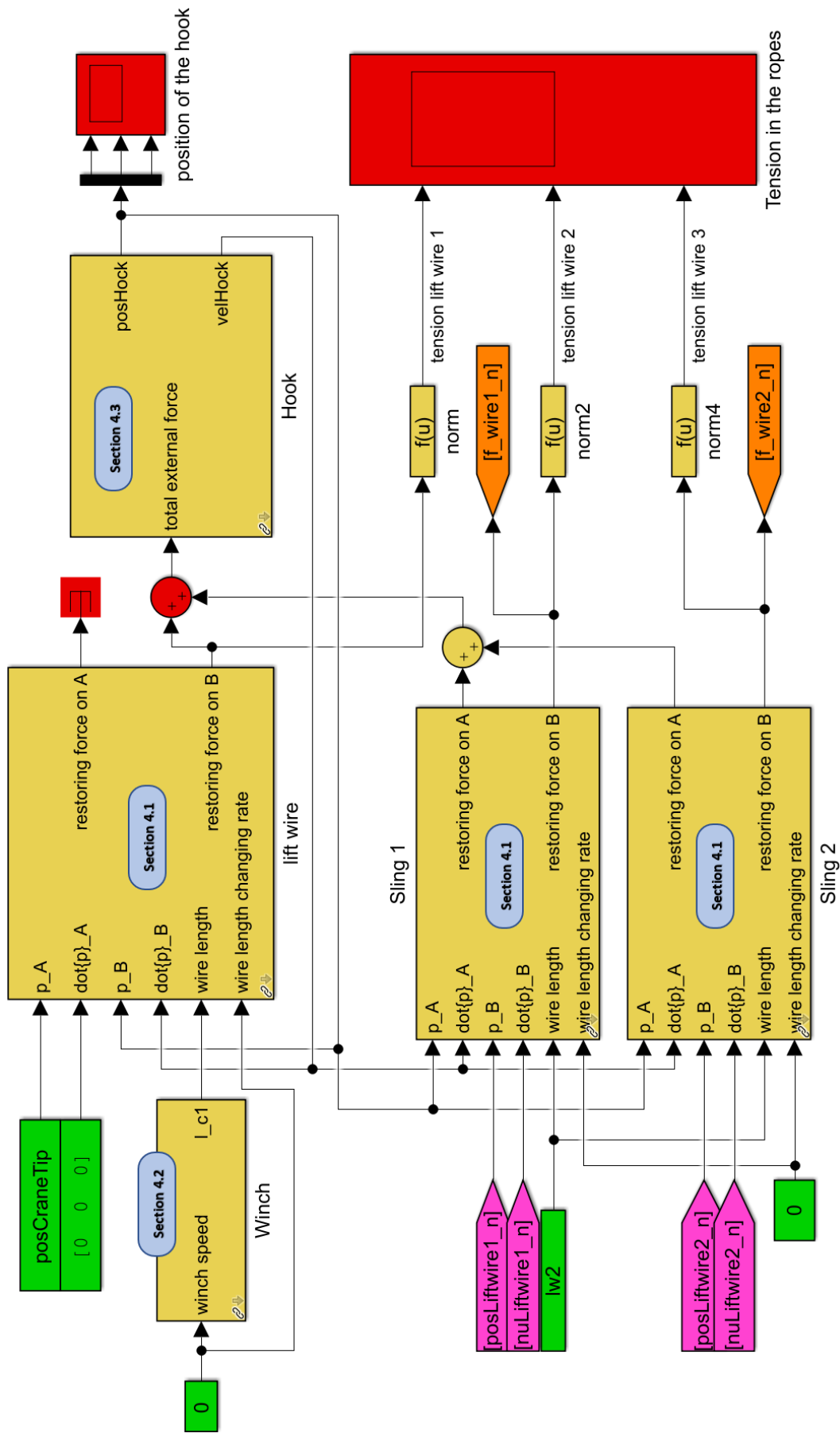
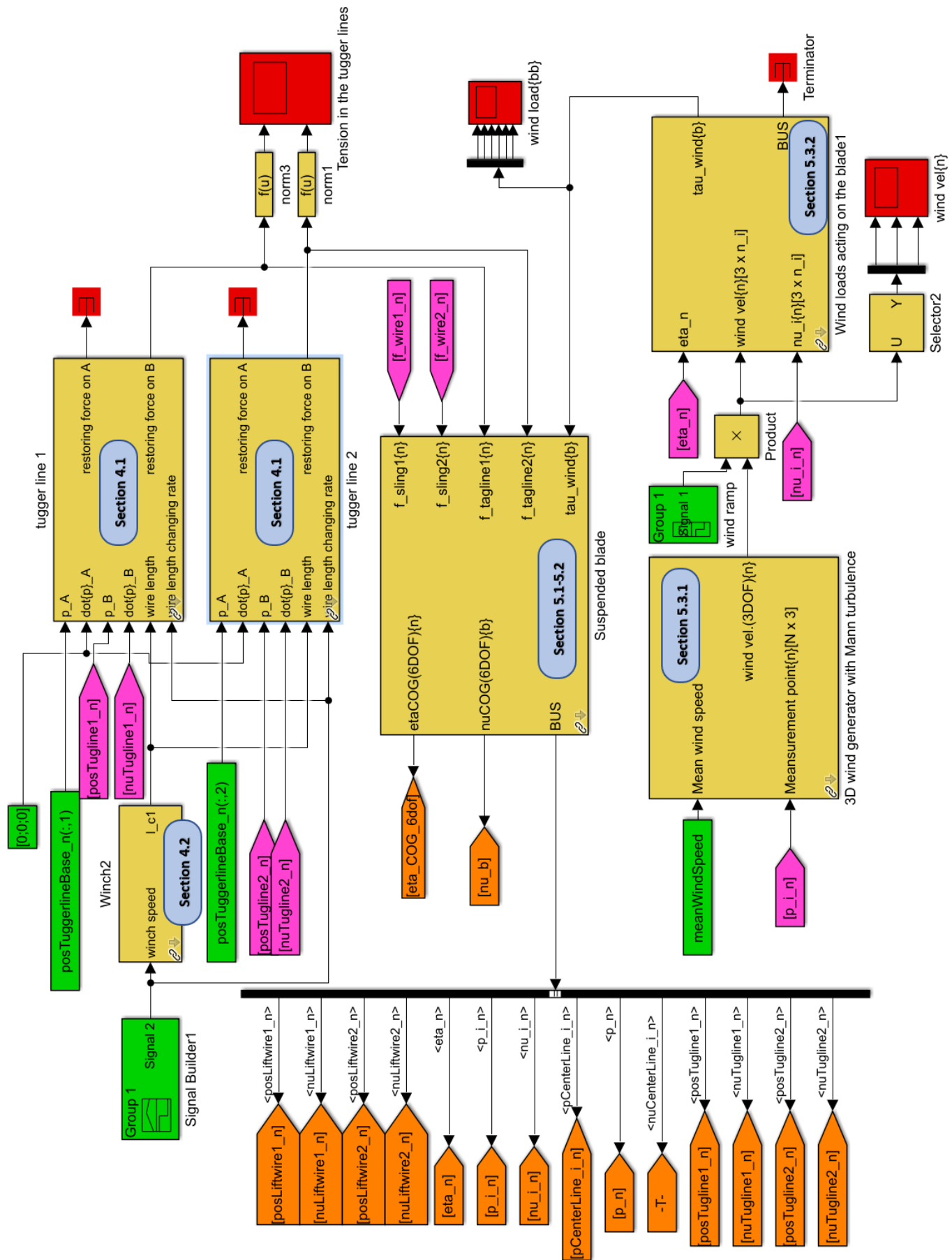Figure B.22: Illustration of the single blade installation model - Part I: lift wire, hook, and slings.

Figure B.23: Illustration of the single blade installation model - Part II: blade, tugger lines, and wind load.

[12] MSS. Marine Systems Simulator, Viewed 30.10.2014, `http://www.marinecontrol.org` (2010).

[13] T. I. Bø, A. R. Dahl, T. A. Johansen, E. Mathiesen, M. R. Miyazaki, E. Pedersen, R. Skjetne, A. J. Sørensen, L. Thorat, K. K. Yum, Marine vessel and power plant system simulator, IEEE Access 3 (2015) 2065–2079.

[14] MARINTEK, SIMO - Theory Manual Version 4.8.4 (2016).

[15] Z. Jiang, T. Moan, Z. Gao, A comparative study of shutdown procedures on the dynamic responses of wind turbines, Journal of Offshore Mechanics and Arctic Engineering 137 (1) (2015) 011904.

[16] T. J. Larsen, A. M. Hansen, How 2 HAWC2, the user's manual, Tech. rep., Risø National Laboratory (2007).

[17] J. M. Jonkman, M. L. Buhl Jr, FAST user's guide-updated august 2005, Tech. rep., National Renewable Energy Laboratory (NREL), Golden, CO. (2005).

[18] E. Bossanyi, Gh bladed user manual, Garrad Hassan Bladed.

[19] J. Jonkman, S. Butterfield, P. Passon, T. Larsen, T. Camp, J. Nichols, J. Azcona, A. Martinez, Offshore code comparison collaboration within iea wind annex xxiii: phase II results regarding monopile foundation modeling, Tech. rep., National Renewable Energy Laboratory (NREL), Golden, CO. (2008).

[20] Z. Jiang, Z. Gao, Z. Ren, Y. Li, L. Duan, A parametric study on the blade mating process for monopile wind turbine installations under rough environmental conditions, Engineering StructuresUnder review.

[21] M. Haastrup, M. R. Hansen, M. K. Ebbesen, Modeling of wind turbine gearbox mounting, Modeling, Identification and Control 32 (4) (2011) 141.

[22] A. Hallanger, I. Ø. Sand, CFD wake modelling with a BEM wind turbine sub-model, Modeling, Identification and Control 34 (1) (2013) 19.

[23] A. Calabretta, M. Molica Colella, L. Greco, M. Gennaretti, Assessment of a comprehensive aeroelastic tool for horizontal-axis wind turbine rotor analysis, Wind Energy 19 (12) (2016) 2301–2319.

[24] RWE Innogy GmbH, Halfway through the turbine installation for the nordsee ost offshore wind farm, `https://www.rwe.com/web/cms/en/113648/rwe/press-news/press-release/?pmid=4012024`, [Online; accessed 16-July-2017] (2014).

[25] J. Jonkman, S. Butterfield, W. Musial, G. Scott, Definition of a 5-MW reference wind turbine for offshore system development, Tech. rep., National Renewable Energy Laboratory, Golden, CO, Technical Report No. NREL/TP-500-38060 (2009).

[26] Z. Ren, R. Skjetne, Z. Gao, Modeling and control of crane overload protection during marine lifting operation based on model predictive control, in: ASME 2017 36th International Conference on Ocean, Offshore and Arctic Engineering, American Society of Mechanical Engineers, 2017, pp. OMAE2017–62003.

[27] K. Feyrer, Wire ropes, Springer, 2007.

[28] O. Egeland, J. T. Gravdahl, Modeling and simulation for automatic control, Vol. 76, Marine Cybernetics Trondheim, Norway, 2002.

[29] T. I. Fossen, Handbook of marine craft hydrodynamics and motion control, John Wiley & Sons, 2011.

[30] J. Diebel, Representing attitude: Euler angles, unit quaternions, and rotation vectors, Matrix 58 (15-16) (2006) 1–35.

[31] J. Mann, Wind field simulation, Probabilistic Engineering Mechanics 13 (4) (1998) 269 – 282. `doi:http://dx.doi.org/10.1016/S0266-8920(97)00036-2`.

[32] N. D. Kelley, B. J. Jonkman, Overview of the TurbSim stochastic inflow turbulence simulator: Version 1.21, Tech. rep., National Renewable Energy Laboratory (NREL), Golden, CO. (2006).

[33] B. J. Jonkman, L. Kilcher, TurbSim user's guide: Version 1.06, Tech. rep., National Renewable Energy Laboratory Colorado (2012).

[34] Turbsim, `https://nwtc.nrel.gov/TurbSim`, accessed: 2017-09-17.

[35] J. D. Anderson Jr, Fundamentals of aerodynamics, Tata McGraw-Hill Education, 2010.

[36] C. Bak, F. Zahle, R. Bitsche, T. Kim, A. Yde, L. Henriksen, P. Andersen, A. Natarajan, M. Hansen, Description of the DTU 10 mw reference wind turbine. DTU wind energy report-i-0092, Technical University of Denmark, Fredericia (Denmark).